Chapter 3
The Quest of Electropromoted Nano-dispersed Catalysts

Arash Fellah Jahromi, Christopher Panaritis, and Elena A. Baranova

Abstract Electrochemical promotion of catalysis (EPOC) also known as non-Faradaic electrochemical modification of catalytic activity (NEMCA) phenomenon of nano-dispersed catalytic systems has been of paramount interest since the pioneering studies of Vayenas and co-workers in the 1980s. A typical heterogeneous catalyst consists of a nano-sized active phase dispersed on high-surface-area support. This allows decreasing the noble metal catalyst loading while considerably increasing the number of surface-active sites available for the reaction. In EPOC studies the catalyst-working electrode is often fabricated as a continuous, porous film with low dispersion; however, more and more works on the fabrication and study of EPOC with nanostructured, dispersed catalysts have emerged recently. This chapter presents a review of EPOC studies with nano-sized, electropromoted catalytic systems reported in the last decade. The first section discusses the origin of EPOC, the main parameters, and the rules. The second part provides the observation of the EPOC effect for both noble and non-noble nanoparticle catalysts. The third part examines recent advances in density functional theory (DFT) for the understanding of electrified interfaces in catalysis, followed by recent advances in self-sustained EPOC. Finally, the last section highlights the research gaps in understanding and applying electrochemically promoted nanostructured catalysts to technologically important processes.

Keywords Electrochemical promotion · NEMCA · Metal-support interaction · Nanoparticle · Heterogeneous catalysis · Nanostructured catalyst · Density functional theory

A. Fellah Jahromi · C. Panaritis · E. A. Baranova (✉)
Department of Chemical and Biological Engineering, Centre for Catalysis Research and Innovation (CCRI), University of Ottawa, Ottawa, ON, Canada
e-mail: afell085@uottawa.ca; cpana054@uottawa.ca; Elena.Baranova@uottawa.ca

P. Vernoux, C. G. Vayenas (eds.), *Recent Advances in Electrochemical Promotion of Catalysis*, Modern Aspects of Electrochemistry 61,
https://doi.org/10.1007/978-3-031-13893-5_3

Abbreviations

ALD	Atomic layer deposition
BZY	$BaZr_{0.85}Y_{0.15}O_{3-\alpha}$
DFT	Density functional theory
DLC	Diamond-like carbon
EDX	Energy-dispersive X-ray
EMF	Electromotive force
EPOC	Electrochemical promotion of catalysis
GO	Graphene oxide
LSCF/GDC	$La_{0.6}Sr_{0.4}Co_{0.2}Fe_{0.8}O_{3-\delta}/Ce_{0.9}Gd_{0.1}O_{1.95}$
LSM/GDC	$(La_{0.8}Sr_{0.2})_{0.95}\ MnO_{3-\delta}/Ce_{0.9}Gd_{0.1}O_{1.95}$
MIEC	Mixed ionic-electronic conductive
MSI	Metal-support interaction
NAS-XPS	Near-ambient pressure X-ray photoelectron spectroscopy
NEMCA	Non-Faradaic electrochemical modification of catalytic activity
NPs	Nanoparticles
P-EPOC	Permanent or persistent electrochemical promotion of catalysis
PM-IRRAS	Polarization modulation infrared reflection absorption spectroscopy
PVD	Physical vapor deposition
PVP	Polyvinylpyrrolidone
RHE	Reversible hydrogen electrode
RWGS	Reverse water-gas shift
SHE	Standard hydrogen electrode
SMSI	Strong metal-support interaction
SRM	Steam reforming of methanol
SSEP	Self-sustained electrochemical promotion
SS-EPOC	Self-sustained electrochemical promotion of catalysis
TGA	Thermogravimetric analysis
TMAOH	Tetramethylammonium hydroxide
TOF	Turnover frequency
tpb	Three-phase boundary
TPD	Temperature program desorption
VOCs	Volatile organic compounds
WGS	Water-gas shift
XAS	X-ray absorption spectroscopy
YSZ	Yttria-stabilized zirconia

3.1 Introduction to Electrochemical Promotion of Catalysis

EPOC or NEMCA phenomenon allows for in situ control of the activity and selectivity of a catalyst towards a favorable reaction rate and products in a reversible manner through the application of electric stimuli (constant current or potential)

[1]. Since the first discovery of the EPOC phenomenon by Vayenas and collaborators [1–3], well over 100 catalytic processes have been studied and demonstrated exceptional enhancement activity and selectivity [4, 5]. As selectivity and activity show a long-life trade-off in heterogeneous catalytic reactions, EPOC can be a noticeable step to resolving and aligning both parameters for reactions and catalysts [6]. To date, the application of EPOC includes, among others, environmental reactions (methane oxidation, abatement of volatile organic compounds (VOCs), and NO_x reduction) [7–11] and production of various chemicals (hydrogen, ammonia, methane, carbon monoxide, etc.) in gas and liquid phases [12–18].

The origin of EPOC is based on the action of ionic promoters' spillover and/or backspillover from the support-solid electrolyte to/away from the deposited catalyst. An electric current or potential is manipulated to control the flux of promoters onto/from the catalyst surface through the three-phase (solid electrolyte-gas) boundary. In a typical EPOC cell, the catalyst-working electrode is polarized using an inert counter electrode that results in the supply/removal of ionic promoters to/from the catalyst surface. This permits to in situ modify the work function of the metal or metal oxide catalyst and as a result its catalytic activity and, in several instances, selectivity in a sustainable and reversible manner. Several promoters have been investigated including positive promoters, e.g., alkali, H^+, and Ag^+, or negative ones, e.g., O^{2-} and F^- [14]. Yttria-stabilized zirconia (YSZ) is the popular choice of solid electrolytes among researchers due to its remarkable stability and bulk ionic conductivity of O^{2-} at temperatures as low as 300 °C [19, 20].

The main parameters to quantify the EPOC phenomenon are the apparent Faradic efficiency (Λ) (Eq. 3.1) and the rate enhancement ratio (ρ) (Eq. 3.2) [4]:

$$\Lambda = \frac{r - r_0}{I/nF} \tag{3.1}$$

$$\rho = \frac{r}{r_0} \tag{3.2}$$

where r_0 is the open-circuit (zero voltage) rate (mol s^{-1}), r is the rate of reaction (mol s^{-1}), I is the current measured across the cell (A), F is Faraday's constant (96,485 C mol^{-1}), and n is the number of electrons. Electrochemical promotion occurs when $\rho \neq 1$ and it is non-Faradic when $|\Lambda| > 1$. The apparent Faradaic efficiency could be below 1 and still indicate the EPOC effect, when the conducting ion from the solid electrolyte does not participate in the electrochemical reaction but alters the catalytic properties (i.e., catalyst work function, oxidation state, surface coverage, etc.) that lead towards the final product [4].

To investigate the behavior of a catalyst under EPOC conditions, it is important to provide information on the electronic properties of the reactants (electron donor or acceptor) [21] and the apparent orders of reaction rate. Therefore, four principal rules were defined to aid in predicting the behavior of the catalytic systems [22]. The four rules were first proposed in [4, 23, 24] and well established in [25]:

R1. Electrophobic (nucleophilic): with an increase in work function (applied potential), the reaction rate shows ascending trend.
R2. Electrophilic: reaction rate exhibits descending behavior with an increase in applied potential.
R3. Volcano-type: the variation of applied potential results in a maximum value and then decreases.
R4. Inverted-volcano type: reaction rate demonstrates a minimum value that ascends once the applied potential varies.

Studies of EPOC reversibility by Comninellis and co-workers led to the discovery of permanent or persistent electrochemical promotion of catalysis (P-EPOC) [26]. In P-EPOC, the catalytic rate after the current/potential interruption is maintained at a higher value than the original open-circuit rate (r_0). The magnitude of the current or potential and the duration of polarization strongly impact the reversibility properties of EPOC [26]. The permanent rate enhancement parameter (γ) (Eq. 3.3), analogous to the rate enhancement ratio of EPOC, is given by

$$\gamma = \frac{r_p}{r_0} \tag{3.3}$$

where r_p is the new steady-state catalytic rate (mol s^{-1}) after potential/current interruption and r_0 is the open-circuit (zero voltage) rate (mol s^{-1}) similar to Eq. (3.2) [26].

Since the year 2000, there are a number of excellent books, book chapters, and comprehensive reviews on the EPOC phenomenon that present and discuss its origin, mechanism, rules, and concept of EPOC, as well as its application to numerous catalytic reactions [14, 27–29]. In this chapter, we focus on reviewing the application of EPOC to nano-sized, highly dispersed catalytic systems published since 2010. In particular, the preparation of mono- and bimetallic nano-catalysts and their implementation into solid-state electrochemical cells for efficient polarization and promotion are discussed. A particular emphasis is made on the functional similarity between metal-support interaction (MSI), also called self-sustained EPOC (SS-EPOC or SSEP), observed between nanoparticles and ionically conductive or mixed ionic-electronic conductive (MIEC) ceramic supports and conventional EPOC phenomenon.

3.2 Electrochemical Promotion of Nanoparticle Catalysts

3.2.1 Pt-Based Nanostructured Catalyst

Nanostructured platinum has been widely investigated in EPOC studies in the last decade thanks to its excellent activity and stability in various reactions, as well as ease of Pt synthesis using various physical (sputtering, physical vapor deposition

(PVD), atomic layer deposition (ALD), etc.) and chemical (chemical vapor deposition, impregnation, polyol method, etc.) techniques. EPOC of Pt nanoparticles was studied for oxidation [30, 31], light alkane production [32, 33], oxidation of aromatic hydrocarbons, e.g., toluene [34], water-gas shift (WGS)/reverse water-gas shift reaction (RWGS) [35, 36], and alcohol synthesis [13] as well as various methane-oriented reactions [37–39].

A pioneering study that employed non-percolated Pt nanoparticles of well-defined size and dispersion was reported by the group of Comninellis and coworkers [4, 31, 39]. In these studies, CO oxidation over electropromoted Pt nanoparticles (NPs), prepared via sputtering deposition, has been studied focusing on fundamental concepts, metal characteristics, supports, and the mode of polarization (bipolar and monopolar) [31, 39]. Pt nanoparticles of the controlled size and size distribution were investigated in the bipolar cell configuration on YSZ (1.7×10^9 Pt particles per cm^2) for CO oxidation at 300 °C [39]. A quantifying method was proposed to distinguish classical electrochemical promotion (EP) from bipolar electrochemical promotion with the aid of isotopically labeled oxygen [39]. Two stages of polarization in the absence and presence of reactive gas were presented. In the absence of reactive gas, only large particles were polarized, whereas increasing the current led to the polarization of smaller particles. With the presence of reactive gas, an equivalent number of completely galvanized cells (n_{cell}) increased and resulted in a boost of the enhancement ratio, as well as CO_2 formation (as indicated by $C^{16}O_2$ and $C^{16}O^{18}O$). However, a considerable difference was observed between the Faradaic efficiency, Eq. (3.2) ($\Lambda = 1.8$) [4], and the modified bipolar efficiency ($\Lambda = 0.086$), where no electrochemical promotion occurs [39]. This behavior was due to nonuniform current distribution and the presence of high local current densities.

Furthermore, Pt nanoparticles of 40 nm average size (1.7×10^9 particles per cm^2 of YSZ) were investigated for CO oxidation [31] where comblike gold electrodes served as a strong electrical field (27,000 Vm^{-1}) at 1μA to polarize Pt nanoparticles. Pt NPs were prepared using sputter deposition following calcination at 700 °C for 4 h. Although only 5% of the active surface area was covered by Pt, the bipolar electrochemical promotion resulted in an enhancement ratio of 500, and operando tuning of catalytic activity was observed at a low current of 0.1μA. As the relaxation step upon current interruption was slow (shown as a slow decrease in the $C^{16}O_2$ and $C^{16}O^{18}O$ formation rate), the electrochemical promotion was determined as a persistent P-EPOC effect [40] where ^{16}O species were stored on the surface as Pt-oxide (PtO_x). Once polarization was relaxed, the stored oxygen species were made available as sacrificial promoters for the reaction [41].

Another significant EPOC breakthrough using highly dispersed Pt NPs catalyst was reported by the group of Vernoux [42]. Pt NPs prepared via wet impregnation on porous $La_{0.6}Sr_{0.4}Co_{0.2}Fe_{0.8}O_{3-\delta}$-$Ce_{0.9}Gd_{0.1}O_{1.95}$ (Pt/LSCF/GDC) were investigated for deep oxidation of propane at low temperatures (267–338 °C) with maximum promotion parameters of $\rho = 1.38$ and $\Lambda = 85$ [42]. The particle size of Pt NPs was in the range of 3 to 20 nm with 15% dispersion. Pt/LSCF/GDC resulted in a remarkable decrease in activation temperature of propane oxidation from 350 °C

to 250 °C in comparison to bare LSCF/GDC. An increase in partial pressure of C_3H_8 from 2200 ppm to 3880 ppm (keeping $P_{O2} = 2.2\%$) resulted in an open-circuit rate enhancement from 2.7×10^{-8} to 19×10^{-8} mol O s^{-1} (or 56%) but only a slight variation in the open-circuit potential (ΔV_{WR}) from −85 to −73 mV in disagreement with solid electrolyte potentiometry (SEP) [43]. The authors concluded that measured potentials and currents for the Pt/LSCF/GDC film corresponded to the electrochemical properties of the LSCF/GDC MIEC layer and not to the Pt NP activity. Under polarization ($I = +200\mu A$), the rate enhancement ratio showed two peaks at 267 °C (Fig. 3.1 (bottom)), while at higher temperatures, one peak was observed. Such results are explained by the low conductivity of LSCF/GDC at relatively low temperatures, which requires time to delocalize the current onto the overall layer of the working electrode. Equally important, the gradual delocalization acts as a proof for homogeneous dispersion of Pt NPs into the LSF/GDF phase.

One of the pioneer studies of active support and EPOC was conducted by the same research group [44]. The authors carried out an investigation of the reaction mechanism of propane combustion over Pt nanoparticles, synthesized with wet impregnation, on YSZ, SiO_2, and ZrO_2. The contribution of the lattice oxygen was investigated using $^{18}O_2$ temperature-programmed desorption (TPD) for all described catalytic systems. Pt deposited on YSZ demonstrated the oxidation of propane by lattice oxygen from YSZ. The strong interaction of nanoparticles and support promoted the state of the catalyst in agreement with the EPOC mechanism.

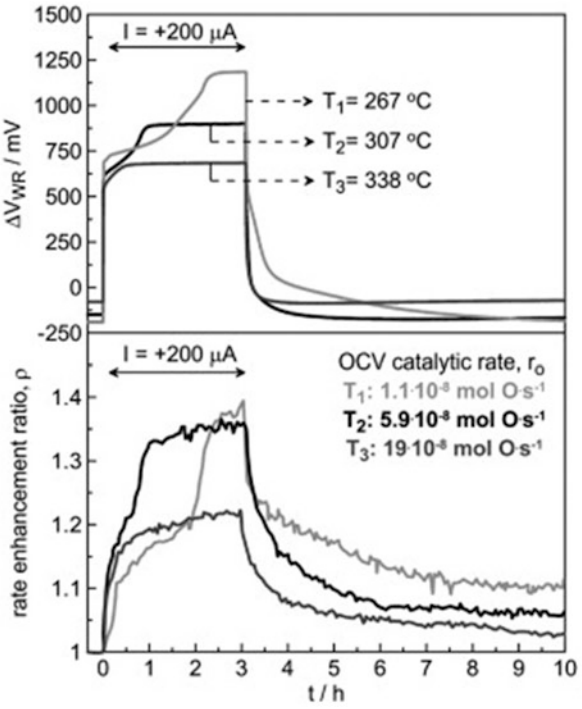

Fig. 3.1 Variation of potential (top) and enhancement ratio (bottom) upon the application of + 200μA at three distinct temperature: $T_1 = 267$ °C, $T_2 = 307$ °C, and $T_3 = 338$ °C. Reactant partial pressure: C_3H_8/O_2: 3880 ppm/2.2%. (Reprinted with permission from Ref. [42], Copyright 2012, Elsevier)

Methanol conversion to hydrogen through steam reforming and partial oxidation was studied using electropromoted nano-dispersed Pt catalysts, deposited by the filter cathodic arc deposition technique [13]. The dispersed Pt NPs (3 nm average size) over diamond-like carbon (Pt-DLC) were deposited on K-β''-Al_2O_3 solid electrolyte. The resulting Pt-DLC underwent high-temperature pre-treatment to attain desirable electrical conductivity. The conductivity increase was confirmed by the scanning transmission microscopy (STEM) and electron energy-loss spectroscopy (EELS) techniques, where the transition from sp^3 carbon into sp^2-hybridized graphitic carbon was observed. The maximum enhancement ratio of 2.5 and 3.5 times was attained under partial oxidation of methanol and steam reforming of methanol (SRM) reactions as a function of H_2 production rate, respectively. The observed steam reforming results were due to the formation of bicarbonate and potassium carbonate promoting species that were also observed using dense Pt films [45]. A comparative study between Pt-DLC catalyst films and pure dense Pt demonstrated that a higher activity was obtained for Pt-DLC due to a lower Pt particle size (3 nm). The maximum enhancement ratio of H_2 for the steam reforming reaction was $\rho = 3.4$ at 360 °C and for partial oxidation was $\rho = 2.5$ at 280 °C. In other studies by de Lucas-Consuegra *et al.*, H_2 production was enhanced 5-fold over dense Pt film [46] for SRM and 6-fold for partial oxidation [45] of methanol using the same NEMCA cell as in [13].

The application of novel techniques for nanoparticle synthesis is important from a fundamental and practical point of view. ALD technique fabricates well-defined nanoparticles and nano-layers. Pt NPs (6.5 nm) were deposited by the ALD on a porous composite backbone fabricated by $(La_{0.8}Sr_{0.2})_{0.95}MnO_{3-\delta}/Ce_{0.9}Gd_{0.1}O_{1.95}$ (LSM/GDC) inspired from solid oxide electrolyte cells (SOEC) [47]. The Pt NPs on LSM/GDC led to a 27% to 33% increase in the catalytic rate (i.e., $\rho = 1.27–1.33$) with respect to the open-circuit and resulted in an apparent Faradaic efficiency between 1000% and 3860% at 300 °C for C_3H_8 oxidation. Long-term stability of 13 h of continuous polarization (100μA) led to a marginal decrease of 5×10^{-10} mol s^{-1} in CO_2 production, signifying a stable conversion. The authors concluded that the catalyst agglomerated at higher temperatures (425 °C) and was in a stable active state [47].

The functional similarity between EPOC and MSI was investigated using Pt and RuO_2 NPs (~2 nm average diameter) for complete ethylene oxidation [48]. The authors synthesized Pt and RuO_x NPs using the polyol reduction method [49] and deposited them directly on the YSZ solid electrolyte disk resulting in free-standing NPs. In addition, the same NPs were dispersed (1 wt.%) on CeO_2, TiO_2, and YSZ powder supports [48] resulting in supported NPs. The closed-circuit reaction rate increased with anodic current (Fig. 3.2a). In addition, the relaxation time (τ), i.e., the time required to reach 63% of steady-state reaction rate under closed-circuit, decreased as a function of current, e.g., 100μA ($\tau = 1.5$ min) and 15μA ($\tau = 5$ min). The enhancement ratio of 1.7 and apparent Faradaic efficiency of 90 were reported for free-standing Pt NPs in this study (Fig. 3.2b).

Only free-standing Pt and RuO_x NPs were electrochemically promoted (Fig. 3.3), while the supported catalysts were already in the promoted MSI state. Figure 3.3

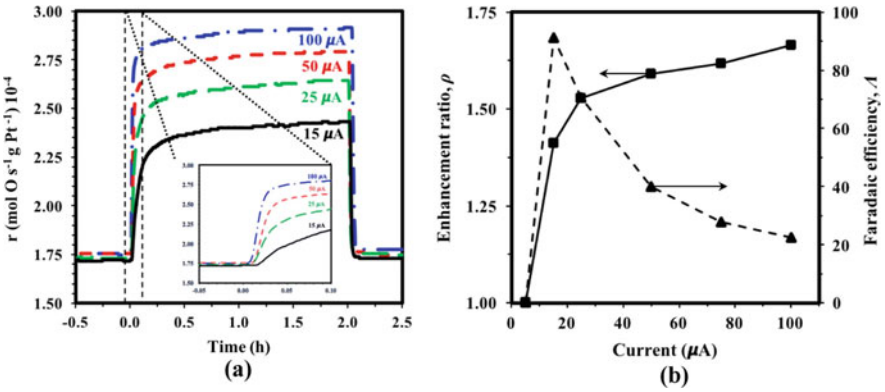

Fig. 3.2 (**a**) Transient rate response of Pt NPs under constant current; (**b**) variation of enhancement ratio ρ and apparent Faradaic efficiency Λ upon applying similar constant current denoted in (**a**). $T = 350$ °C, 3 kPa of O_2 and 0.012 kPa of C_2H_4, flow rate of 100 mL min^{-1}. (Reprinted with permission from Ref. [48], Copyright 2017, Elsevier)

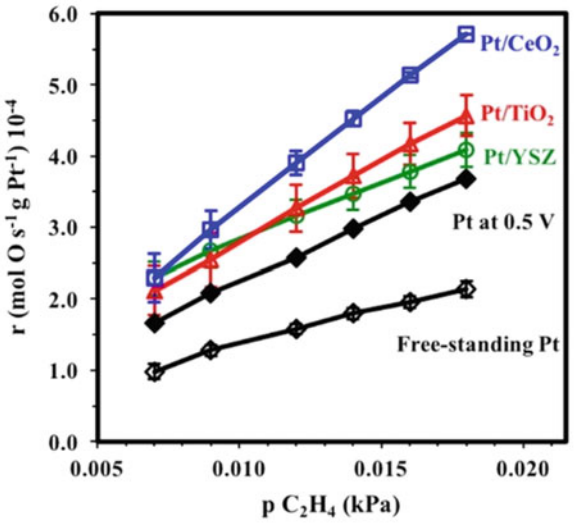

Fig. 3.3 Catalytic rate vs. partial pressure of C_2H_4 for: Pt-based NPs (free-standing and supported). Experimental conditions: $T = 350$ °C, 3 kPa of O_2 and various partial pressures of C_2H_4 as indicated in the figure, and flow rate of 100 mL min^{-1}. (Reprinted with permission from Ref. [48], Copyright 2019, Elsevier)

shows that the specific reaction rate increased with increasing C_2H_4 partial pressure for all Pt catalysts, where the reaction rate of unpromoted free-standing Pt NPs was the lowest and increased significantly under polarization or by interfacing Pt with active ionic ceramic supports. A comparable degree of promotion was achieved under open-circuit conditions for dispersed Pt NPs on CeO_2, TiO_2, and YSZ supports and EPOC of free-standing Pt NPs. These findings further confirmed the functional equivalence of EPOC and MSI with highly dispersed Pt NPs.

Therefore, the synthesis and application of size-controlled mono- and bimetallic NPs for electrochemical promotion studies in the last decade led to the advancement and better understanding of the MSI phenomenon, in particular, the MSI mechanism with ionically and mixed ionic-electronic conducting supports that will be discussed later in Sect. 4 [5]. The summary of EPOC studies with Pt NPs is shown in Table 3.1.

3.2.1.1 Pd-Based Nanostructured Catalyst

Palladium (Pd) has been widely studied for catalytic reaction development, particularly for energy and environmental application. Pd is the most active metal for the complete oxidation of methane in conventional heterogeneous catalysis and in EPOC studies [4, 52–56]. Recently, EPOC of nanostructured Pd films [37] deposited inside a monolith honeycomb (600 channels) YSZ (8 mol% Y_2O_3) solid electrolyte was reported for deep methane oxidation. Pd NPs were deposited into the YSZ monolith via the electroless plating technique reported earlier [50]. A maximum electrochemical promotion of Pd/YSZ under oxidizing conditions of CH_4/O_2: 2%/10% and under −2 V resulted in $\Lambda = 47$ at 400 °C. In this study, electrochemical promotion was observed at both negative and positive potentials [52].

In the work of Matei et al. [51], Pd NPs (8 nm average size) were prepared by the impregnation method on YSZ solid electrolyte of different porosity for complete methane oxidation. The authors demonstrated that a more porous YSZ increased the activity of Pd towards methane combustion due to a 4.5-time increase in the catalyst dispersion when compared with dense YSZ [51]. The porosity of the support impacted the transformation between metallic Pd and more active PdO_x. Another study [9] reported EPOC of Pd NPs synthesized via polyol method (average particle size of 5–35 nm) and deposited on YSZ for methane oxidation. Both positive and negative polarization at relatively low temperatures (340 °C) resulted in the reaction rate increase. Enhancement under negative polarization was explained by competitive adsorption of CH_4 and O_2 under stoichiometric, reducing, and oxidizing conditions. This competitive adsorption was mechanistically explained by the formation of PdO_x which can be limited at low O_2 partial pressure (<5 kPa). Higher oxygen partial pressure resulted in the full coverage of the catalyst surface and blockage of CH_4 adsorption sites leading to a decrease in the reaction rate.

Zagoraios et al. [52] evaluated EPOC of Pd/Co_3O_4 nanoparticles (4 nm average size) prepared by the polyol method for complete methane oxidation. To this end, Pd colloidal NPs were dispersed on commercial porous Co_3O_4 semiconductor powder and deposited on YSZ solid electrolyte disk. Pd/Co_3O_4 was compared to a Pd thin film (1.5 mg cm^{-2}) prepared using Pd commercial paste (Engelhard A1121). The open-circuit catalytic activity for Pd/Co_3O_4 was 12 times higher than the Pd film. Under anodic polarization, the catalytic rate of the Pd film increased 12-fold, while for Pd/Co_3O_4, the catalytic rate increased 2-fold. Pd/Co_3O_4 required half the time to reach a promoted state over the Pd film, due to the shorter diffusion path over the nanoparticles. Even though the Pd film experienced a higher electrochemical promotion effect, the overall catalytic activity for Pd/Co_3O_4 outperformed Pd film. Pd

Table 3.1 Examples of nano-dispersed electropromoted Pt catalysts

Catalyst	Synthesis or deposition method	Reaction	Electrolyte	Reactants	ρ	Λ	Total flow and/or reactant mixture	T (°C)	Ref. and year
Pt	Sputtering	CO oxidation	YSZ	CO, O_2	≤ 2	1.8	High vacuum	300	[39], 2010
Pt	Sputtering	CO oxidation	YSZ	CO, O_2	500	1.5	High vacuum	300	[31], 2011
Pt	Wet impregnation	C_3H_8 oxidation	LSCF/GDC	C_3H_8, O_2	1.38	85	C_3H_8/O_2: 2200 ppm and 3880 ppm/2.2%	267–338	[42], 2012
Pt	Filter cathodic arc deposition technique	CH_3OH steam reforming (SR) and partial oxidation (POX)	K–$\beta''Al_2O_3$	CH_3OH, O_2; CH_3OH, H_2O	SR: 3.4 @ 360 °C; POX: 2.5 @ 280 °C	–	6 L. h^{-1} CH_3OH/H_2O: 4%/4.8%; CH_3OH/O_2: 11%/0.9%	250–360	[13], 2013
Pt	Wet impregnation	C_3H_8 combustion	YSZ; SiO_2; ZrO_2	C_3H_8, O_2	–	–	1.8 L. h^{-1}	25–600	[44], 2014
Pt	Atomic layer deposition	C_3H_8 oxidation	LSM/GDC	C_3H_8, O_2	1.27–1.33	10–38.6	6 L. h^{-1} P_{C3H8}/P_{O2}: 0.22 kPa/2.2 kPa	300	[47], 2017
Pt	Polyol reduction	C_2H_4 oxidation	YSZ	C_2H_4, O_2	1.8	23	6 L. h^{-1} P_{C2H4}/PO_2: 0.012 kPa/3 kPa	350	[48], 2017

nanoparticles deposited on Co_3O_4 powder resulted in an MSI which enhanced the catalytic properties of Pd/Co_3O_4 by cycling oxygen during open-circuit conditions and directing oxygen and electrons under polarization.

Persistent EPOC (P-EPOC) was observed during methane oxidation over Pd NPs (5 nm average size), synthesized using the polyol method [53]. EPOC of Pd NPs on YSZ solid electrolyte showed an electrophobic behavior with an apparent Faradaic efficiency of 3000 (at $I = 1\mu A$) and a maximum rate enhancement ratio of $\rho = 2.7$ under a 2 kPa and 4 kPa gas composition of CH_4 and O_2, respectively (Fig. 3.4). The degree of p-EPOC increased with polarization time due to the continuous increase in the amount of O^{2-} stored in the PdO_x active phase [53]. The relationship between the duration of polarization and the time required to obtain the initial value of the open-circuit rate is shown in Fig. 3.4a (insert) with a slope of 0.5, along with the corresponding current (Fig. 3.4b). Thus, p-EPOC occurred due to the stored oxygen ions in PdO_x that acted as sacrificial promoters when polarization was interrupted.

Bimetallic nano-sized catalysts have attracted considerable attention, to achieve bi-functionality to increase and/or stabilize the catalytic activity and reduce the amount of noble metals [54, 55]. EPOC of the bimetallic Ni9Pd (90:10 at% of Ni to Pd) nanoparticles was studied for the complete oxidation of methane [54]. The Ni9Pd NPs were synthesized using a modified polyol method and deposited on the YSZ disk. The resulting structure of NPs was a core double-shell with Pd located at the core, Ni as the inner shell, and a second 3- to 4-nm-thick Pd outer shell (Fig. 3.5) [54]. Such a structure significantly enhanced the catalytic activity and stability under open-circuit when compared with monometallic Ni and Pd. The EPOC was observed under positive polarization in a reversible and controllable manner that increased the reaction rate by 240% ($\rho = 2.4$) at 425 °C (Fig. 3.6a). The highest promotion was attained under fuel-rich conditions if compared to fuel-lean and stochiometric gas composition. This catalytic system met economic and performance criteria, where

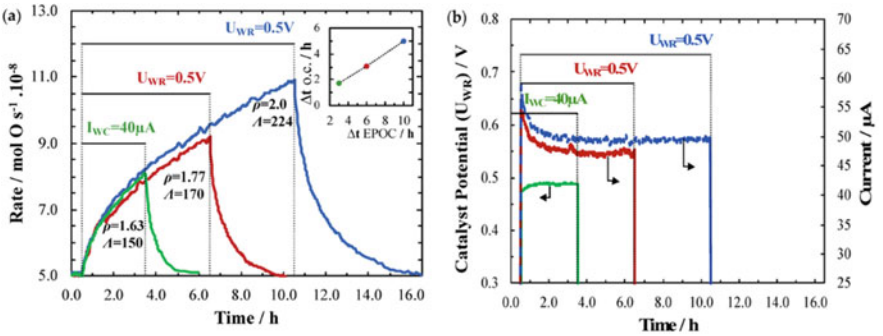

Fig. 3.4 (**a**) Transient rate response of Pd/YSZ polarized for 3.5 h, 6.5 h, and 10.5 h. Insert in (**a**) time after polarization to reach the initial open-circuit as a function of polarization time; (**b**) corresponding potential/current recorded at potentiostatic or galvanostatic application. Conditions: $T = 425$ °C, 2 kPa of CH_4 and 4 kPa of O_2, and flow rate of 100 mL min^{-1}. (Reprinted under an open access Creative Common CC BY license from Ref. [53], Copyright 2019, Molecular Diversity Preservation International)

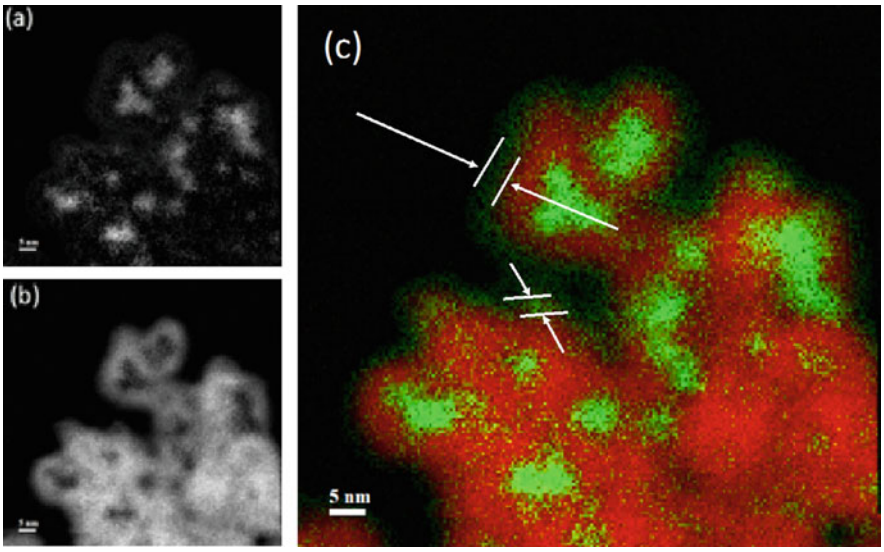

Fig. 3.5 HAADF STEM-EELS and element mapping under different signal range showing (**a**) Pd at signal range: 364.3–468.0 eV, (**b**) Ni at signal range: 848.0–885.8 eV and (**c**) illustration of double-shell structure (colored coded map) with Pd (green) as the core, Ni (red) inner shell, and Pd outer shell with average particle size of 3–4 nm. (Reprinted with permission from Ref. [54], Copyright 2019, Elsevier)

the costly Pd phase was minimized while maintaining the high active surface area and synergistic interaction between Ni and Pd. A maximum rate enhancement ratio and Faradaic efficiency of 1.3 and 39, respectively, occurred at $U_{WR} = 0.25$ V and P_{O2}/P_{CH4} ratio of 0.1 (Fig. 3.6b).

Electrochemical promotion of Pd was also investigated for CO_2 hydrogenation [56] and electrochemical CO_2 reduction reactions [57] with the goal of waste carbon dioxide utilization and transformation to useful chemicals, such as CO [56], formate [57], or methane [58]. CO_2 hydrogenation reaction pathways vary over different catalysts under atmospheric pressure, such as RWGS, methanation, or conversion to formate in aqueous media [57]. CO_2 hydrogenation was studied by Bebelis *et al.* over a thin-film coating of Pd (A1122 Engelhard Pd paste) on solid electrolytes YSZ and Na-$\beta''Al_2O_3$ [56]. Only the RWGS reaction was observed at 533 °C and 605 °C for a CO_2/H_2 ratio of 1:2.3. For Pd/YSZ, the RWGS was enhanced under anodic and cathodic polarization indicating an "inverted-volcano" behavior. For Pd/β''-Al_2O_3, the RWGS rate increased under negative polarization where Na^+ is supplied to the gas-exposed catalyst surface resulting in a 6-time rate increase. This behavior is explained by the coverage increase of the Na positive promoter and simultaneous drop of the catalyst work function. Consequently, the CO_2 adsorption was enhanced leading to an increase in the CO formation rate.

Electrochemical promotion of Pd NPs for CO_2 electroreduction in an aqueous 1 M $KHCO_3$ solution saturated with H_2/CO_2 was reported recently [57]. The Pd NPs

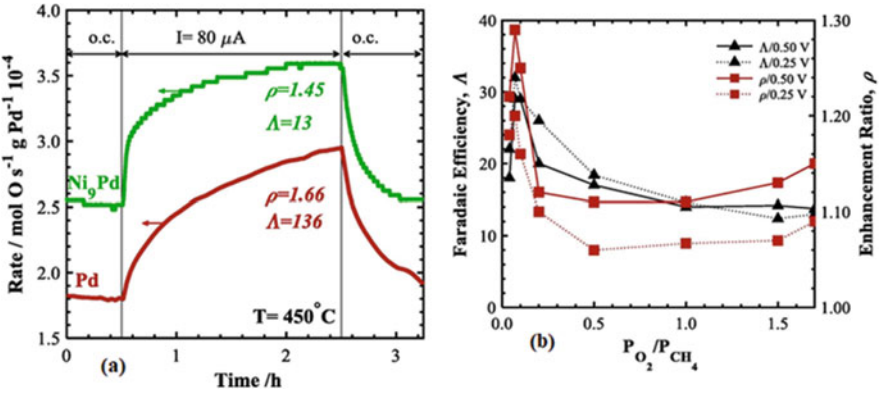

Fig. 3.6 (**a**) Catalytic rate response of Pd and Ni9Pd upon the application of $I = 80\mu A$. Experimental condition: $T = 450\ ^{\circ}C$, $P_{CH4} = 2$ kPa, $P_{O2} = 4$ kPa, and He balanced. (**b**) Enhancement ratio and apparent Faradaic efficiency obtained for Ni9Pd as a function of step change of U_{WR} to 0.25 V and 0.5 V, respectively. Experimental conditions: $T = 450\ ^{\circ}C$, $P_{CH4} = 10$ kPa, and a variable P_{O2}/P_{CH4} ratio. (Reprinted with permission from Ref. [54], Copyright 2019, Elsevier)

with an average particle size of 3.7 nm were synthesized using the sodium borohydride reduction method. The catalyst layer was composed of a catalyst ink of Pd/C and Nafion ionomer deposited on carbon paper (Toray TGP-H-060). The experiments were carried out in an H-type electrochemical cell (Fig. 3.7a) under ambient temperature. Working and counter electrode cell compartments were separated by a Nafion 115 membrane. Both electrochemical and catalytic reduction of CO_2 took place over Pd/C. Electrochemical promotion of Pd/C catalyst under negative polarization (in the range of −0.1 and −0.4 vs. RHE) showed that the formate production rate increased between 10 and 143 times depending on the Pd particle size and applied potential (Fig. 3.7b). Electrochemical polarization activated H_2 from the electrolyte solution and stabilized the active phase of PdH_x to promote catalytic CO_2 reduction. Authors suggested that electrocatalytic and catalytic reduction of CO_2 shared the same $HCOO^*$ intermediate that resulted in formate rate increase [57]. The reaction mechanism was explained by the weakening of the hydrogen adsorption bond on PdH_x under negative polarization, at an optimal value of −0.2 V with respect to the maximum enhancement ratio. The relationship between NP size and enhancement ratio is illustrated in Fig. 3.7b [57]. Decreasing the particle size increased the enhancement ratio for all applied potentials.

In a recent work [59], catalytic non-Faradaic CO_2 hydrogenation to formate in aqueous media was significantly enhanced via polarization. The reaction rate of formate production increased by three orders of magnitude due to local pH changes under polarization. Small polarization affected a nonequilibrium local environment in the vicinity of the electrode, leading to a coexistence of high alkalinity and high CO_2 concentration. The local pH changes were different from the electrolyte bulk, where alkalinity and CO_2 concentration were inversely correlated. These early works on CO_2 hydrogenation in aqueous media [57, 59] show a significant potential of the

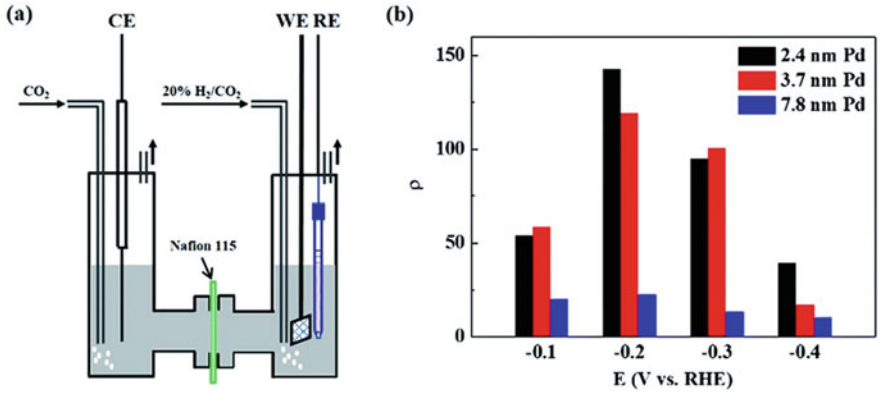

Fig. 3.7 (**a**) Schematic of the H-cell for CO_2 reduction. (**b**) Rate enhancement ratios for formate production at different negative potentials for Pd NPs with an average size of 2.4 nm, 3.7 nm, and 7.8 nm in 20% H_2/CO_2-saturated 1 M $KHCO_3$ solution under ambient temperature. (Reprinted from Ref. [57] licensed under a Creative Commons Attribution 3.0 Unported License (materials can be used without requesting further permissions); Copyright 2017, The Royal Society of Chemistry)

EPOC phenomenon for the field of CO_2 conversion and utilization not only in the gas phase but also in liquid-phase catalytic reactions in combination with electrocatalysis. Table 3.2 shows the summary of some examples of electropromoted Pd NPs catalysts that were discussed in Sect. 3.2.2.

3.2.2 Ru-Based Nanostructured Catalyst

Free-standing RuO_2 nanoparticles (0.8 nm average size) deposited on YSZ solid-electrolyte were studied for the complete ethylene oxidation [61]. The catalyst was evaluated experimentally and theoretically, using DFT calculations to provide an atomistic understanding of the role of O^{2-} in promoting RuO_2. Free-standing RuO_2 nanoparticles [62] were synthesized through the polyol method using tetramethylammonium hydroxide (TMAOH) to adjust the pH. Under reaction conditions ($P_{C2H4} = 0.012$ kP and $P_{O2} = 3$ kPa), the CO_2 rate increased under both positive and negative polarization or otherwise followed an inverted-volcano EPOC behavior (Fig. 3.8a, b). Theoretically, RuO_x structures were examined as a function of potential and oxygen coverage, correlated to the experimental data. The DFT part of this work is discussed in detail in Sect. 3.3.

Ruthenium is active for CO_2 hydrogenation reactions because it can activate CO_2 and H_2, to produce CH_4 and CO through the methanation and RWGS, respectively. Kotsiras *et al.* [63] studied nano-dispersed Ru-Co nanoparticles (6–8 nm) deposited on an interlayer Ru film (2.1 mg cm^{-2}) on the proton conductor (H^+) barium zirconia yttria-doped (BZY, $BaZr_{0.85}Y_{0.15}O_{3-\alpha}$ + 1 wt% NiO) solid electrolyte for CO_2 hydrogenation [63]. The Ru-Co nanoparticles were synthesized on BZY powder

Table 3.2 Examples of nano-dispersed electropromoted Pd catalysts

Catalyst	Synthesis or deposition method	Reaction	Electrolyte	Reactants	ρ	Λ	Total flow and/or reactant mixture	T (°C)	Ref. and year
Pd	Impregnation	CH_4 oxidation	Porous YSZ	CH_4, O_2	1.2 @ 400 °C	6 @ 400 °C	6 L. h^{-1} P_{CH4}/PO_2: 1.3 kPa/4.5 kPa	350–430	[51], 2013
Pd	Wet impregnation	CH_4 oxidation	YSZ	CH_4, O_2	5	~32	3 L. h^{-1} P_{CH4}/PO_2: 1 kPa/5 kPa	340	[9], 2018
Pd	Polyol reduction	Complete methane oxidation	YSZ	CH_4, O_2	2.7	3000	6 L. h^{-1} PCH_4/PO_2: 2 kPa/4 kPa	425	[53], 2019
Ni9Pd	Modified polyol	Complete methane oxidation	YSZ	CH_4, O_2	2.4	25	P_{CH4}/PO_2: 10 kPa/1 kPa	425	[54], 2019
Pd	Thin coating	RWGS	YSZ; Na–β″Al_2O_3	CO_2, H_2	YSZ: 6.1 @ Na–β Al_2O_3: 6.7 @ 605 °C	–	P_{CO2}/P_{H2}: 2.1–3.5	533–605	[56], 2008
Pd	Sodium borohydride reduction	CO_2 reduction (aq. rxn.) to formate	1 M $KHCO_3$	CO_2, H_2	10–143	–	20% H_2/CO_2 saturated	Ambient	[57], 2017
Pd	Pre-fabricated Pd/C (fuel cell store [60])	CO_2 hydrogenation to formate	50 mM $KHCO_3$/0.5 M $NaClO_4$	CO_2, H_2	3	–	H_2/CO_2: 20%/80%	Ambient (24 ± 1)	[59], 2020

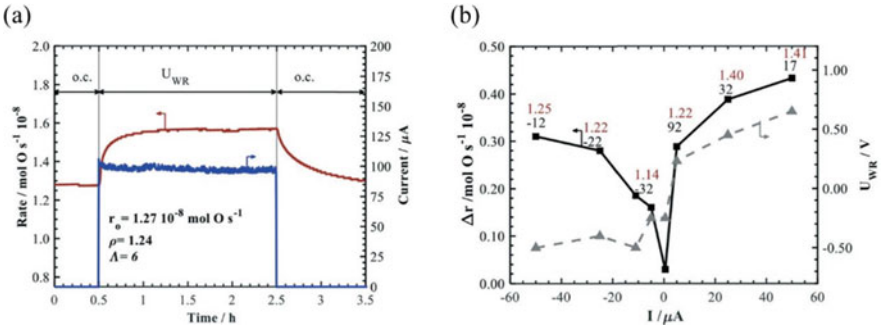

Fig. 3.8 Transient reaction rate response of free-standing RuO_2 nanoparticles (**a**) under $U_{WR} = 1$ V and (**b**) summary of the rate enhancement ratio as a function of potential. Experimental conditions: $T = 350$ °C, $P_{C2H4} = 0.012$ kPa, $P_{O2} = 3$ kPa, and total flow rate = 100 mL min^{-1}. (Reprinted with permission from Ref. [61], Copyright 2020, Elsevier)

via the wet impregnation method. The interlayer Ru film was used to disperse the Ru-Co nanoparticles, ensuring electrical contact and closing the circuit. The selectivity to CO was 84% due to the spontaneous migration of protons backspilling over on Ru-Co at 450 °C and CO_2/H_2 ratio of 1:7. Under 1.5 V the Ru-Co/BZY/Ru deposited on BZY solid- electrolyte promoted the methanation rate ($\rho = 2.7$) and suppressed the CO rate ($\rho = 0.8$) while under −1.5 V promoted the methanation ($\rho = 1.1$) and CO rate ($\rho = 1.05$).

In another study [16, 62], RuO_2 nanoparticles (0.8 nm average size) were deposited on YSZ and BZY solid electrolytes and evaluated for the CO_2 hydrogenation reaction in the temperature range of 250 °C to 400 °C. Under open-circuit conditions and a CO_2/H_2 ratio of 1:7, Ru nanoparticles were selective to CO (>75%) over CH_4, which was assigned to the small size of the nanoparticles and high dispersion on the solid electrolyte. Positive polarization increased the CH_4 production rate ($\rho = 1.8$ and 1.5 for YSZ and BZY, respectively) and suppressed CO formation. Negative polarization decreased the CH_4 rate and minimally affected the CO rate. The same electrochemical behavior was observed regardless of the type of solid electrolyte and followed the same results when a Ru film of 3μm was deposited on YSZ, BZY, Na-Al_2O_3, and K-Al_2O_3 solid electrolytes [63–66].

3.2.2.1 Rh-Based Nanostructured Catalyst

The first EPOC studies of the rhodium (Rh) nanostructured catalyst electrode for ethylene complete oxidation were reported in the early 2000s [67–69]. Recently, an elegant work by Katsaounis et al. [70] reported a fundamental study on the dependency of the Rh oxidation state and its stability under polarization using near-ambient pressure X-ray photoelectron spectroscopy (NAP-XPS). To this end, a Rh nano-film (thickness of <40 nm) catalyst was sputtered on a YSZ solid electrolyte (Rh/YSZ) using DC magnetron sputtering. NAS-XPS results revealed that the

supply of oxygen ions onto the pre-oxidized Rh surface promotes the shift to a metallic state by facilitating the reduction of the Rh surface under C_2H_4. Thus, a Rh oxide layer (RhO_x, $x < 2$) is present and stabilized under certain experimental conditions.

Closed-circuit results were examined at a potential difference of 1.5 V between the Rh catalyst-working electrode and counter electrode and continuous current flow. The mixture ratio (oxidizing, stoichiometric, and reducing) versus the current reveals that the stoichiometric ratio ($C_2H_4/O_2 = 0.33$) secured the maximum value of current (+100μA) as the optimal partial oxide layer was formed. Under reducing conditions ($C_2H_4/O_2 > 0.33$), the current decreased. Thus, RhO_x surface films can be stabilized under mild reducing and stoichiometric mixtures. This study provided spectrometric evidence to support the contribution of anodic polarization on the pre-oxidized Rh surface and the alteration of surface oxidation and subsequent reduction step from RhO_x to Rh metallic. This observation is in line with the sacrificial promoting ion model for EPOC and MSI [4, 71, 72].

3.2.2.2 Au-, Ag-, and Cu-Based Nanostructured Catalyst

Gold (Au)-based catalysts were disregarded for many years since they were viewed as inert and inactive in heterogeneous catalysis and in EPOC application. Haruta et al. [73–75] demonstrated that Au is active in the nanoparticle range (≤10 nm). In recent years, several studies on the electrochemical promotion of Au NPs have been reported [79–82]. González-Cobos et al. [76] promoted Au nanoparticles towards the partial oxidation of methanol. The catalytic system consisted of a 7% atomic weight of Au (3.3 nm, synthesized via magnetron sputtering) supported on a thin film (170 nm) of YSZ. Then, the Au-YSZ catalyst was deposited on the K-β″Al_2O_3 solid electrolyte. Catalytic measurements were conducted under $CH_3OH/O_2 = 5.9\%/0.43\%$ at 280 °C. Au nanoparticles resulted in a promising selectivity towards methyl formate ($HCOOCH_3$) and H_2 with a five- and nine-fold increase in production rate with respect to open-circuit conditions, respectively [77–79]. Analysis of the results revealed that the observed EPOC effect was only sensitive to the rate of K^+ supply and coverage. The optimal promoter coverage was 0.5 at 280 °C and $V_{WR} \leq -0.5$ V and resulted in an enhancement ratio of 9, 2, and 5 for H_2, CO_2, and $HCOOCH_3$ production, respectively.

Silver (Ag)-based catalysts have been widely used to study the EPOC effect since its discovery and in recent studies [80]. Ag nanoparticles deposited via evaporative PVD on a YSZ solid electrolyte were characterized through cyclic voltammetry to study the growth of silver oxides in the vicinity of the three-phase boundary. The results demonstrated that both anodic and cathodic polarization affected the oxidation state of Ag, where anodic polarization contributed to the formation of Ag_2O over metallic Ag [81]. Kalaitzidou et al. developed an Ag-coating film (10–25μm thickness) electrochemical cell using the screen-printing deposition on YSZ to study the EPOC effect of propylene combustion [82]. The authors showed that high catalytic activity towards propylene conversion is attainable under the high coverage

of propylene and oxygen over the surface of the catalyst-working electrode (Ag). The highest enhancement ratio ($\rho = 1.34$) was obtained by applying +25μA under lean-burn conditions, whereas stoichiometric conditions gave the highest enhancement ratio equal to 1.03 under +2μA polarization. The promotion was amplified under lean-burn (oxidizing atmosphere) conditions. This technology can aid in the abatement of propylene from the air.

Table 3.3 summarizes EPOC studies with Ru-, Rh-, Au-, and Ag-based nanoparticles for various catalytic processes.

Copper is an economic option in comparison with noble metals such as Pt, Rh, Pd, and Ru and can be an attractive catalytic system in EPOC studies. González-Cobos et al. [83] studied the electrochemical promotion of Cu deposited on K-β″Al_2O_3 for the partial oxidation of methanol to produce H_2 at a relatively low temperature of 320 °C. Nanostructured Cu was prepared via oblique angle physical vapor deposition with a thickness of ~0.8μm, a porosity of ~50 nm, and a nanocolumn cross-sectional diameter of 120 nm. The applied polarization ($I < 0$ and $V_{WR} = 0$ with $V_{ocp} \leq +0.5$ V) resulted in a remarkable enhancement in catalytic activity and a subsequent three-fold increase in production rates of methyl formate ($C_2H_2O_2$) and H_2 ($\rho_{max} = 2.7$ for $C_2H_2O_2$, $\rho_{max} = 2.63$ for H_2). The work function of Cu decreased due to the migration of positive promoters (K^+) and enhanced the reaction. These species altered the chemisorption of the O_2 molecules (electron acceptor) in a favorable manner upon the consumption of CH_3OH. The post-mortem energy-dispersive X-ray (EDX) and XPS characterization determined that the electropromoted state caused the formation of potassium-derived by-products (K_xO_y and/or carbonates).

In another study, Ruiz et al. [84] conducted a bench-scale study on CO_2 hydrogenation over Cu nanoparticles deposited on K-β″Al_2O_3 solid electrolyte. Cu nanoparticles with an average diameter of 23 nm were deposited on K-β″Al_2O_3 using electroless deposition. The reactant ratio of H_2/CO_2 was modified to 2, 3, and 4 based on post-combustion CO_2 capture exit streams to investigate the practical application and scalability of the process. The results revealed that the determining parameter to control selectivity was affiliated to Cu^+ ions and large Cu particles that were selective towards CH_3OH and an unconventional selectivity to CH_4 and CO. Selectivity values of C_2H_6O, CH_3OH, and C_2H_5OH were boosted by a maximum of 34%, 340%, and 220% via polarization (in a range between −2 and 4 V). The optimal reaction temperature was 325 °C, and the maximum selectivity was attained by a feed ratio of H_2/CO_2 of 2:1. Selectivity of dimethyl ether decreased with an increase in the reactant ratio. Thus, this study is one of the forward steps for EPOC commercialization because the flow rate was high (522 L h^{-1} = 8700 mL min^{-1}), and industrial feed ratios were selected.

In a recent study, EPOC of Cu NPs deposited on the YSZ was investigated for RWGS. Cu NPs of 20 nm average size were synthesized via the polyol method and deposited on the YSZ disk [85]. Only positive polarization increased RWGS, and the highest rate increase occurred under +2 V at a CO_2/H_2 ratio of 1:1 at 400 °C. The resulting rate enhancement ratio (ρ) was 1.2, and the Faradaic efficiency (Λ) was

Table 3.3 Examples of nano-dispersed electropromoted catalyst from Sects. 3.2.3, 3.24 and 3.2.5

Catalyst	Synthesis or deposition method	Reaction	Electrolyte	Reactants	ρ	Λ	Total flow and/or reactant mixture	T (°C)	Ref. and year
RuO_2	Polyol reduction	Complete C_2H_4 oxidation	YSZ	C_2H_4, O_2	1.24	6	3 L. h^{-1} P_{C2H4}/PO_2: 0.012 kPa/3 kPa	350	[61], 2019
Ru-Co	Wet impregnation	CO_2 hydrogenation	BZY	CO_2, H_2	CO: 0.8, CH4: 2.7 @ 1.5 V; CO: 1.1, CH4: 1.05 @ −1.5 V	–	12 L. h^{-1} P_{CO2}/P_{H2}: 1 kPa/7 kPa	450	[63], 2018
RuO_2	Wet impregnation	CO_2 hydrogenation	BZY	CO_2, H_2	CH_4: 1.5 @ 350 °C	CH_4: 8.6 @ 350 °C	6 L. h^{-1} P_{CO2}/P_{H2}: 1 kPa/7 kPa	250–400	[16], 2020
RuO_2	Polyol reduction	CO_2 hydrogenation	YSZ	CO_2, H_2	CH_4: 1.8	CH_4: 34	6 L. h^{-1} P_{CO2}/P_{H2}: 1 kPa/7 kPa	250	[62], 2020
Rh	DC magnetron sputtering	C_2H_4 oxidation	YSZ	C_2H_4, O_2	–	–	P_{C2H4}/PO_2: 0–9 (reducing: 0.3, oxidative: 3.6	400	[70], 2018
Au-YSZ	Magnetron sputtering	CH_3OH partial oxidation (POX)	K–$\beta''Al_2O_3$	CH_3OH, O_2	H_2: 9; CO_2: 2; $HCOOCH_3$: 5	–	6 L. h^{-1} CH_3OH/O_2: 5.9%/0.43%	280	[76], 2014
Ag	Screen-printing	C_3H_6 oxidation	YSZ	C_3H_6, O_2	Lean-burn: 1.34; stoichio.: 1.03	Lean-burn: 137; stoichio.: 571	Stoichio.: 6 L h^{-1} and C_3H_6/O_2: 0.1%/0.45%; Lean-burn: 3 L. h^{-1} and C_3H_6/O_2: 0.1%/3.6%	300	[82], 2018

6.52. TEM, XPS, and cyclic voltammetry confirmed the active state of Cu as Cu_2O and CuO indicating that the reaction over Cu/YSZ followed the redox mechanism.

3.2.2.3 Ni-, Fe-, and Co-Based Nanostructured Catalyst

Nickel is an alternative to noble metals and economically preferable over noble metal catalysts [54, 86, 87]. Various Ni catalyst electrodes have been studied for a number of reactions deposited on solid electrolytes supplying positive [88–91] or negative promoters [54].

Nickel electrode deposited using oblique angle PVD on K-$\beta''Al_2O_3$ was applied in methanol steam reforming. The research group of de Lucas-Consuegra [89] studied the contribution of formed graphene oxide on H_2 storage and production during methanol steam reforming over Ni at 280 °C. The proposed mechanism was based on the chemisorption of H_2 on the active sites of Ni and the role graphene oxide (GO) had on the spillover of H_2 under the K^+ promotion effect. Such a porous catalytic system increased the possibility of GO aggregate formation, whereas H_2 storage and production were controlled by varying current/potential under fixed experimental conditions.

In another study, Espinos et al. [90] elucidated the EPOC mechanism over alkaline ionic conducting materials via the in situ near-ambient pressure photoemission (NAP) spectroscopy technique. They revisited the migration of K^+ ions with regard to diffusion of positive promoter ions or their reduction, by applying various polarization modes. It was proposed that ions adsorbed at the three-phase boundary had two different modes of transport: (i) onto the surface of the catalyst exposed to reactants and (ii) into the inner interfaces or grain boundaries of the catalyst. Both modes are at equilibrium where backward and forward migration continuously take place; however, the first mode of transport is favorable with respect to energy.

As one of the early works on Ni deposited on alkali (K^+) solid electrolytes, de Lucas-Consuegra et al. [91] investigated the water-gas shift reaction ($T = 350$ °C and CO/H_2O ratio of 1:3) over Ni NPs (100 nm and film dispersion of 0.84%). The authors observed that with negative polarization, K^+ ions migrated onto the catalyst surface to promote the selectivity towards CO and H_2 with an increase in the H_2 catalytic rate ($\rho_{H2} = 2.7$). The reversibility of the EPOC effect can be explained by the activation of the chemisorption process for H_2O molecules and subsequent generation of OH species.

In the most recent research conducted over Ni-based catalysts [88] for CO_2 hydrogenation, three catalyst-working electrodes were investigated with respect to CO_2 and CH_4 production: (i) Ni/K-$\beta''Al_2O_3$, (ii) Ni-αAl_2O_3/K-$\beta''Al_2O_3$ (40 mg Ni, 20 mg α-Al_2O_3, and ethylene glycol), and (iii) Au-Ni (30%)-αAl_2O_3/K-$\beta''Al_2O_3$ (mixture of 40 mg Au ink and 20 mg α-Al_2O_3 previously impregnated with Ni (30%)). The mean particle diameter (after reduction through TPR) of the first sample (denoted as sample N) was 39.9 nm, whereas the particle size of the second sample (labeled as NA) and the third sample (labeled as GNA) was 37.5 and 35.2 nm, respectively. The authors showed that with the addition of α-Al_2O_3 to NA, the

dispersion of Ni was improved, and all samples were porous (based on SEM analysis) which remarkably enhanced the diffusion of reactants and products. NA catalyst showed the highest activity explained by an increase in the porosity of the catalyst film (composed of Ni). In addition, the CO formation rate was dependent on two parameters: (i) a direct relationship with the CO_2 feed and (ii) an inverse variation with changes in applied potential (where a decrease in potential resulted in an increase in the CO production rate). Although CO formation gave promising results under negative polarization, CH_4 production was favored by introducing positive potential (spillover of K^+ onto solid electrolyte and removal from the catalyst surface). In addition, increasing H_2 concentration (electron donor) demonstrated a positive impact on CH_4 production due to its electrophilic nature. Finally, the rate of consumption of CO_2 profoundly increased, and the EPOC effect exhibited a reproducible and reversible trend.

Progress towards the use of transition metals has been pioneered in the use of nanostructured FeO_x catalysts for the RWGS reaction. Monometallic FeO_x nanowires ($Ø = 5$ nm) deposited as a nano-film on YSZ solid electrolyte responded to the application of polarization with a CO rate increase of 200% ($\rho = 2$). FeO_x nanowires were synthesized through the polyol synthesis method with TMAOH. This was the first EPOC study where non-noble metal nanostructured catalysts were studied to electrochemically activate FeO_x for the RWGS reaction. Under open-circuit conditions, the CO_2 conversion varied as a function of temperature, relating to the oxidation state of FeO_x. XPS and cyclic voltammetry (CV) characterization provided insight on the state changes of FeO_x cycling between $Fe_2O_3 \rightarrow Fe_3O_4 \rightarrow FeO \rightarrow Fe \rightarrow Fe_xC$ from −1.6 eV to 1.6 eV (U_{WR}) under a CO_2/H_2 ratio of 1:1 (Fig. 3.9a) [17]. Figure 3.9b [17] summarizes an interesting electrochemical response to the application of $U_{WR} = 2$ V at 350 °C. A potential difference of 2 V initially electrochemically oxidized Fe-carbide that was formed during open-circuit conditions. As polarization continued, FeO_x was saturated with oxygen (Fe_3O_4/FeO), reaching an active state to favor RWGS. Once polarization was interrupted, the stored oxygen in FeO_x was made available for the RWGS reaction resulting in a P-EPOC for 5 h. FeO_x is active for the RWGS reaction as Fe_3O_4, FeO, and Fe, while Fe_2O_3 and Fe_xC phases are inactive. The efficiency of the RWGS reaction was ensured by the in situ control of the oxidation state. To evaluate the presence of the Fe_xC phase, CO_2 and H_2 were left to react on FeO_x for 12 h and then replaced by He, and polarization then supplied Fe_xC with oxygen to produce CO in the absence of CO_2. Additionally, negative polarization led to a $\rho = 2.4$ and $\Lambda = 4$ at 350°C, following inverted-volcano behavior. Overall, this study showed how the oxidation state of Fe can be manipulated electrochemically to favor the RWGS catalytic reaction. The advantage of the inverted-volcano effect is the increase in catalytic rate during positive and negative polarization that allows the counter and working electrodes to be composed of the same metal, where both sides are efficiently promoted under polarization.

In another study [92], FeO_x nanowires decorated by Ru clusters (20 at.%) have been shown to inhibit Fe_xC formation, allowing FeO_x to remain in an oxide state during open-circuit conditions (Fig. 3.10 [92]). The Ru/FeO_x catalyst was

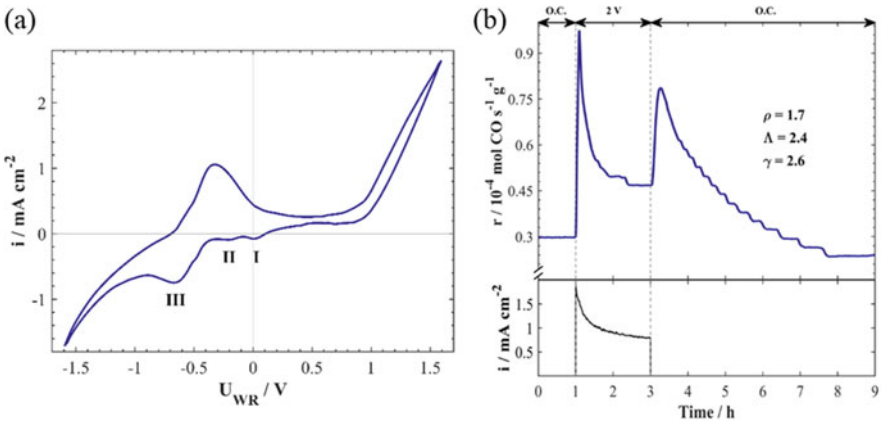

Fig. 3.9 Cyclic voltammetry of FeO_x nanowires deposited on YSZ under reaction conditions at 350 °C (**a**) stable CV and (**b**) transient response at 350 °C for 2 V under reaction conditions and current response. $CO_2/H_2 = 1{:}1$, and 100 mL min^{-1}. (Reprinted with permission from Ref. [17]; Copyright 2020, Elsevier)

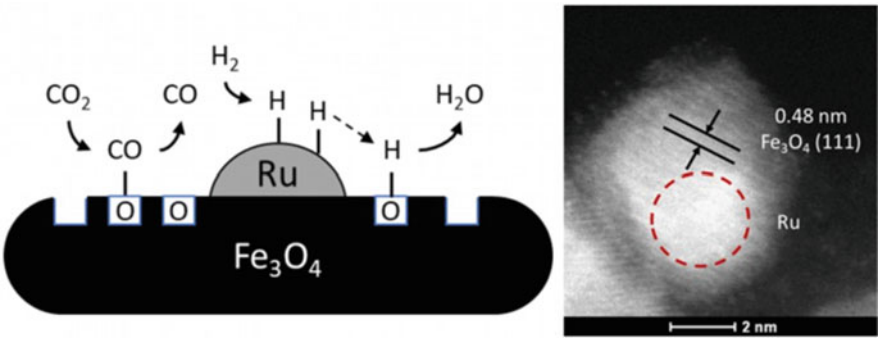

Fig. 3.10 Mechanism of the RWGS reaction on the Ru/FeO_x catalyst. (Reprinted with permission from Ref. [92]; Copyright 2020, Elsevier)

synthesized through a two-step polyol method where FeO_x nanowires were first synthesized followed by Ru clusters reduced on FeO_x. Polarization of Ru/FeO_x led to a reversible catalytic rate increase of $\rho = 2.4$. Positive polarization shared a similar response to FeO_x with the absence of the initial CO rate. Ru inhibited the formation of Fe_xC by ensuring it remained as Fe_3O_4, as shown in the STEM images. The presence of Ru was shown to favor the adsorption of H_2 and its dissociation into H, where it can spill over onto FeO_x to keep it oxidized.

Zagoraios et al. [93] studied free-standing Co nanoparticles (20 nm) synthesized through the polyol method deposited on YSZ and BZY for the RWGS reaction. XPS and imaging characterizations confirmed that polarization affected the work function and oxidation state of the Co catalyst surface. Figure 3.11 [93] displays the transients

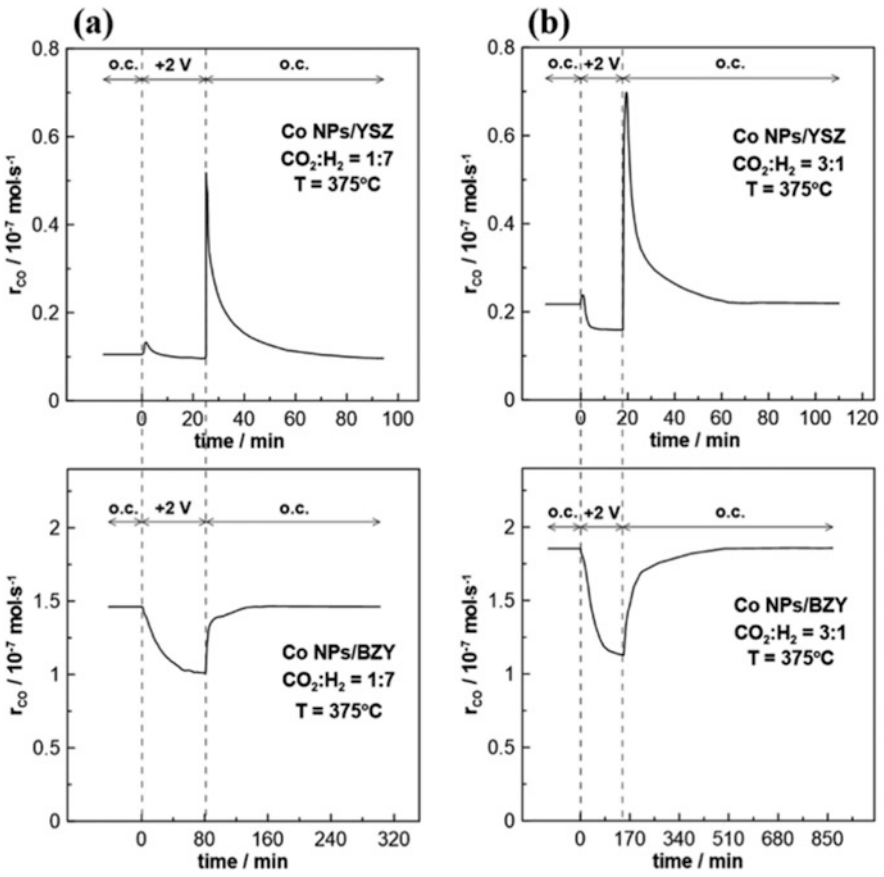

Fig. 3.11 Transient rate response of Co nanoparticles under 2 V polarization for (**a**) Co NPs/YSZ and (**b**) Co NPs/BZY, under reducing and oxidizing conditions at 375 °C. (Reprinted with permission from Ref. [93]; Copyright 2020, American Chemical Society)

of Co nanoparticles deposited on YSZ (O^{2-}) and BZY (H^+) under a potential difference of 2 V. For YSZ, the CO rate decreased as CoO_x was fully oxidized, followed by a spike in the catalytic CO rate of 650%, once potential was interrupted. Similar to FeO_x on YSZ, oxygen is stored as CoO_x and made available for the reaction. In the case of BZY, the CO rate response followed the kinetic behavior of the RWGS reaction and the absence of the post-polarization promotion. Regardless of the type of ionic species, the RWGS reaction for Co nanoparticles followed electrophilic behavior. The authors showed with XPS characterization that Co_3O_4 is dominant on the Co nanoparticles exposed to gaseous oxidation, while for 2 V polarization a mixed $Co^{2+,3+}/Co^{2+}$ state was formed. XPS confirmed that polarization affected the oxidation state of the Co nanoparticles providing a method to tailor the catalytic activity to favor the RWGS reaction. This study supports the unique

behavior exhibited by transition metals that are influenced by polarization to tailor the reaction.

Table 3.4 summarizes EPOC studies over Cu, Ni, Fe, and Co nanoparticles for various catalytic processes that were discussed in Sects. 3.2.5 and 3.2.6.

3.3 Study of EPOC Using Density Functional Theory

DFT is a unique tool to elucidate the atomic nature of the catalytic reaction. Numerous studies have been conducted using DFT calculations to supplement experimental results; however, only a handful have rationalized the EPOC effect [94–96]. Atomic slabs of Pt(111), RuO_2(110), and Ru(0001) were used to simulate small, free-standing Pt, Ru, and RuO_x nanoparticles (1–3 nm) and to establish a computational method to evaluate the EPOC effect by using the surface charging method or grand-canonical DFT [61]. Polarization was simulated through the addition and removal of electrons following the linearized Poisson-Boltzmann equation from VASPsol. Omitting many computational details, this method is used to control the number of electrons for the metal, which modifies the surface charge and work function of the slab. The model is not limited to the type of reaction since it affects the properties of the metal and the molecules.

The first study to apply the electrochemical model was on the RuO_2 (110) surface, where it was used to describe the electrochemical behavior of RuO_x nanoparticles for the complete oxidation of C_2H_4 [61]. The surface energies were measured as a function of potential and oxygen surface coverage. DFT calculations confirmed that under positive polarization simulated conditions (removal of electrons) facilitate the cleavage of the C–C bond to activate C_2H_4 on the RuO_2 (110) surface. Under negative polarization, DFT confirmed O_2 dissociation as the rate-limiting step justifying the inverted-volcano behavior. Thus, DFT calculations identified how polarization affected the binding energy of each molecule.

To provide insight into the origin of the "two oxygen species" that were demonstrated upon positive polarization through XPS, TPD, and cyclic voltammetry characterizations over Pt catalyst-working electrode [97–99], DFT calculations were carried out using Pt(111) slab for the complete oxidation of CH_4 [100]. The hypothesis was that one species originated from YSZ, while the other one was from the gas phase, relating to one oxygen atom on Pt(111) and α-PtO_2, respectively. DFT calculations were compared alongside the experimental methane oxidation reaction, where the reaction followed inverted-volcano behavior (i.e., catalytic rate increased under positive and negative application). Pt(111), 0.25 monolayer (ML) of O on Pt (111), and α-PtO_2 on Pt(111) were evaluated under the influence of polarization and are summarized in Fig. 3.12 [100], in the potential difference range of −1 to 1 U/V vs SHE. Evaluating the activation energy (E_a) of methane on the surface, above $U_{WR} > 1$ U/V vs SHE, the most stable surface was α-PtO_2 on top of Pt(111). In the range of 0 to 1 U/V vs SHE, one oxygen atom (0.25 ML) on Pt(111) was the most stable, which displayed the highest E_a. While for negative polarization, the Pt(111)

Table 3.4 Examples of nano-dispersed electropromoted catalysts (Sects. 3.2.5 and 3.2.6)

Catalyst	Synthesis method	Reaction	Electrolyte	Reactants	ρ	Λ	Total flow and/or reactant mixture	T (°C)	Ref. and year
Cu	Electroless deposition	CO_2 hydrogenation	K–β″ Al_2O_3	CO_2, H_2	C_2H_6O: 3.4; CH_3OH: 34; C_2H_5OH:22	–	522 L. h^{-1} H_2/CO_2: 2, 3, 4	325	[84], 2014
Cu	Oblique angle physical vapor deposition	CH_3OH partial oxidation (POX)	K–β″ Al_2O_3	CH_3OH, O_2	$C_2H_2O_2$: 2.7; H_2: 2.63	–	6 L. h^{-1} CH_3OH/O_2: 4.4%/0.3%	320	[83], 2015
Cu	Polyol	RWGS	YSZ	CO_2, H_2	1.2	6.52	6 L. h^{-1} H_2/CO_2: 1:1	400	[85], 2022
Ni	Thermal decomposition	WGS	K–β″ Al_2O_3	CO, H_2O	H_2: 2.7	–	6 L. h^{-1} CO/H_2O: 1:3	350	[91], 2011
Ni	Deposition	CO_2 hydrogenation	K–β″ Al_2O_3	CO_2, H_2	CO_2: 1–2, CO: 1–3.2, CH_4: 0.5–1	–	6 L. h^{-1} H_2/CO_2: 30%: 1.5%	240	[88], 2015
FeO_x	Polyol	RWGS	YSZ	CO_2, H_2	1.7 @ +2 V	2.4 @ +2 V	6 L. h^{-1} H_2/CO_2: 1:1	350	[17], 2020
FeO_x −20 at.% Ru	2-step polyol	RWGS	YSZ	CO_2, H_2	2.4	0.5	6 L. h^{-1} H_2/CO_2: 1:1	350	[92], 2020
Co	Polyol	RWGS	YSZ; BZY	CO_2, H_2	YSZ: 6.5	–	6 L. h^{-1} H_2/CO_2: 7:1	350	[93], 2020

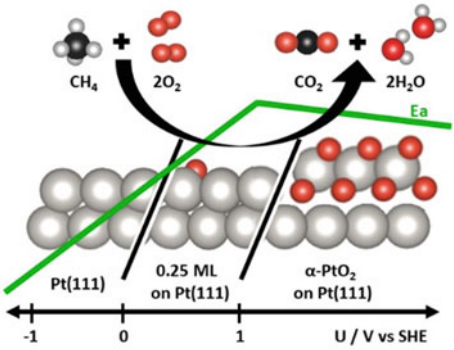

Fig. 3.12 Summary of the Pt(111) surface for the CH_4 oxidation reaction as a function of potential and oxygen coverage with corresponding activation energy (E_a). The Pt(111) is strongly influenced by polarization resulting in the change in activation energy of the reaction. (Reprinted with permission from Ref. [100]; Copyright 2020, American Chemical Society)

surface is favored. The initial hypothesis was that Pt(111) favors the dissociation of O_2, but the E_a energy was lower than CH_4 in the whole potential range. Thus, the authors concluded that the inverted-volcano effect was affiliated with the surface state change influenced by the potential conditions. When compared with the experimental E_a energies [101], the theoretical trend lines up with the negative application, while the positive is not as steep and is affiliated to other oxide surfaces that have not been evaluated. Thus, decades after the discovery of the NEMCA/EPOC effect, DFT calculations provide a way to back up the experimental observations.

Furthermore, the CO_2 hydrogenation reaction was evaluated on the Ru(0001) slab to elucidate the EPOC effect of Ru where positive polarization led to CH_4 formation and negative polarization led to CO formation regardless of the type of ionic species in the solid electrolyte. DFT calculations were performed without taking into account the type of ionic species (i.e., O^{2-}, H^+, Na^+, K^+); instead only polarization is analyzed by adding and removing electrons on Ru(0001). The intermediates were evaluated as a function of potential where the binding energy of the CHO and CO molecules was discovered to influence the selectivity of the reaction (Fig. 3.13) [62]. For positive polarization, CO is strongly adsorbed increasing its hydrogenation towards CH_4, by enhancing the adsorption strength of the CHO* intermediate. For negative polarization, the CO bond is weakened allowing it to likely desorb. The energies under the influence are close in value, which further explains the selectivity between CH_4 and CO for a Ru catalyst. Thus, a universal mechanism for Ru (nanoparticles, sputtered, thick porous layer, etc.) influenced by polarization can be used to model and simulate electrochemical polarization and its behavior.

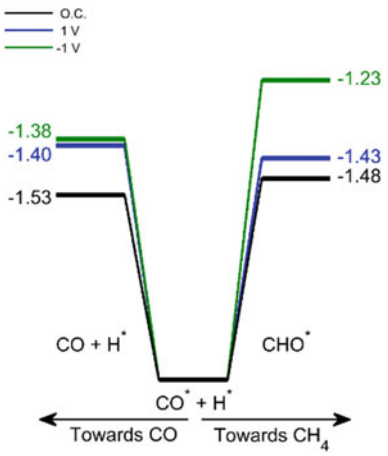

Fig. 3.13 Branching of the CO* + O* intermediate towards CO and CHO* as a function of potential at 250 °C on Ru(0001) for CO_2 hydrogenation. Energies provided in eV. (Reprinted with permission from Ref. [62]; Copyright 2020, Elsevier)

3.3.1 Recent Advancement of Self-Sustained Electrochemical Promotion

Metal-support interaction (MSI) and EPOC have long been considered two different phenomena in heterogeneous catalysis; however, in the last two decades, it has been shown that, functionally, MIEC and ionic conducting materials, both phenomena are linked by the transfer of ionic species at the metal-ceramic interfaces. Understanding the metal-support interaction and its link with EPOC was first observed in 2001 in collaborative work between the research groups of Vayenas, Verykios, and Comninellis [102]. In this work, the reaction of ethylene complete oxidation was investigated over a highly dispersed Rh catalyst deposited on TiO_2, γ-Al_2O_3, WO_3-doped TiO_2, SiO_2, and YSZ supports. In addition, a Rh thin-film catalyst-working electrode was deposited on YSZ for EPOC experiments. The application of potential to the Rh catalyst-working electrode resulted in similar behavior to Rh dispersed on supports, proving how EPOC can be functionally like the MSI effect, where EPOC is in situ controlled via electrochemical stimuli (see Fig. 1.12). In the MSI effect, the conducting supports (e.g., CeO_2, TiO_2) not only enhance catalyst dispersion but also change the catalyst properties by changing the d-bond centers of the surface (metallic state) that interact with the oxide support. The strong metal-support interaction (SMSI) initially coined by Tauster [103–106] implies the coverage of nanoparticles by suboxides that originate from the support under reducing conditions [103–105, 107]. These suboxides are recognized as atomic layers with a presumably amorphous character. A trade-off between the blockage of active sites by suboxides and alteration of local electronic structures was investigated, and the latter case outweighs the former as the role of suboxides as Lewis acids caused the activation of reactants and subsequent tuning of the catalytic performance [108].

Furthermore, extensive research on the functional similarity of EPOC and MSI with ionic and MIEC catalyst supports has been carried out in the last decade. The first confirmation of the existence and the role of ionic species (O^{2-}) from the support was reported by Vernoux et al. in the instance of Pt deposited on a YSZ powder support for deep propane oxidation [109]. The authors used TPD to study the oxidation state of nano-dispersed Pt synthesized via the impregnation method on YSZ support. Three states were determined via TPD (Fig. 3.15): state (I) TPD spectrum under 1 h exposure of oxygen to the surface of the fresh Pt/YSZ at 300 °C, state (II) spectrum recorded after cooling down to 300 °C and again exposure to oxygen for 1 h (following the completion of the first state and increasing the temperature to 700 °C), and state (III) spectrum taken after cooling down to 500 °C and exposing to oxygen for 1 h, cooling down to 300 °C and subsequent exposure to 1% O_2 for 1 h, and lastly cooling down to room temperature under oxygen purging. Catalytic measurements were carried out under the conditions of states II and III with 2000 ppm C_3H_8 and 1% O_2. The TPD analysis showed the presence of $O^{\delta-}$ at 595 °C that was assigned to $O^{\delta-}$ from YSZ support (state I) in agreement with the previous studies by Katsaounis et al. [110] and Li et al. [111]. Catalytic results under states II and III showed that O^{2-} species were thermally induced and originated from YSZ, which resulted in a strong promotion of propane deep oxidation (Fig. 3.14). Thermal migration of O^{2-} was proven by TPD analysis for propane combustion over Pt/YSZ and can be considered as a key step for advancing the understanding of the MSI with ionically conducting ceramics as active supports. The effect was coined self-sustained electrochemical promotion (SS-EPOC or SSEP) to indicate that this is MSI with ionically conductive supports, where the charge transfer occurs via ionic species that migrate to the gas-exposed catalyst surface to modify its properties. SS-EPOC or MSI for a Pt/YSZ catalytic

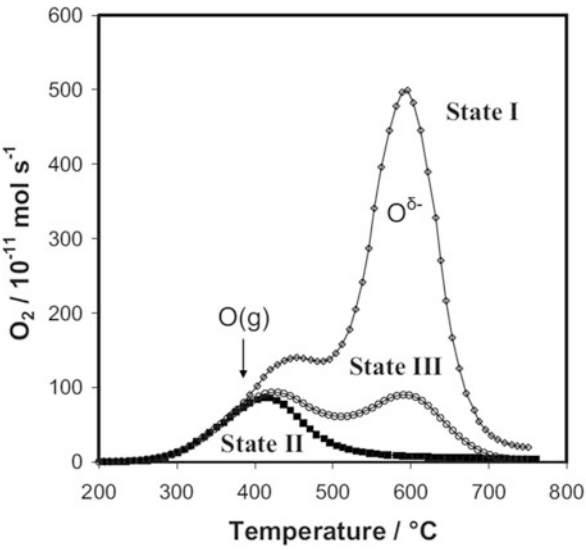

Fig. 3.14 Spectra of O_2– TPD taken after O_2 adsorption over Pt/YSZ (powdered). (Reprinted with permission from Ref. [109]; Copyright 2009, IOP Science)

system was demonstrated for CO, C_2H_4, and toluene oxidation reactions [30, 34, 112, 113].

The charge transfer and modification of the catalyst electronic state were confirmed by ex situ XPS investigations of Pt NPs deposited on YSZ powder support [114]. Pt nanoparticles with four different average sizes ranging from 1.9 to 6.7 nm were dispersed on YSZ powder. For all catalysts, the Pt4f peak was found at lower binding energies compared to the position of the peak of a Pt bulk foil. The Pt4f XPS peak shifted by as much as 0.9 eV for the smallest Pt NPs compared to the peak position of the Pt foil. In addition, changes were found on the Y3d, Zr3d, and O1s spectra after Pt nanoparticle deposition. All these confirmed a charge transfer from the oxide support to the Pt NPs and that this effect was particle size dependent, where the highest electronic modification was observed for the smallest catalyst (Fig. 3.15).

The particle size effect on the extent of MSI [115] was investigated over Pt/YSZ powder catalyst for the oxidation of CO and C_2H_4 in oxygen-free and oxygen-rich environments. In this work, Pt nanoparticles of various average sizes were synthesized via the polyol method and deposited as 1 wt% on YSZ powder. This work demonstrated that oxygen ions from the support take part in the reaction even at temperatures below 100 °C. The proposed mechanism for CO and C_2H_4 oxidation in the absence of oxygen in the gas feed was explained through the formation of local nano-galvanic cells in the vicinity of the three-phase boundary (tpb). In the spontaneous nano-galvanic cell, the oxidation of CO and C_2H_4 was accompanied by the electroreduction of zirconia. The smallest Pt NPs with a mean diameter of 1.9 nm displayed the highest activity and turnover frequency (TOF), whereas no activity was observed for larger particle size (6.7 nm) in an oxygen-deficient environment (Fig. 3.16). As for the oxygen-rich environment, the reaction took place at a lower temperature. Two contributing oxidizing mechanisms under oxygen-rich conditions were proposed: (i) thermally induced backspillover of O^{2-} from YSZ to the surface of the catalyst (metal/gas interface) and (ii) electroreduction at the three-phase boundary.

Furthermore, the effect of the ionically conducting support, i.e., pure ionic (YSZ or SDC) vs. MIEC (CeO_2) and non-conducting γ-Al_2O_3 and carbon black, was studied for ethylene and carbon monoxide oxidation over Pt NPs (2.5 nm average size) [8]. To this end, 1 wt% of Pt NPs was deposited on YSZ, CeO_2, SDC ($Sm_{0.2}Ce_{0.8}O_{1.9}$), γ-Al_2O_3, and carbon black [8]. Catalytic activity measurements showed that Pt/C and Pt/γ-Al_2O_3 were both inactive under a zero-oxygen environment, whereas the rest of the samples exhibited high catalytic activity in the oxygen-deficient environment with complete oxidation of CO and C_2H_4 below 220 °C. The highest catalytic activity for C_2H_4 oxidation was observed for Pt/SDC, explained by the higher bulk ionic conductivity of SDC [8] and the facile oxygen release from CeO_2 if compared to YSZ. The surface O^{2-} resulted in electrochemical oxidation of CO and C_2H_4 by O^{2-} in the vicinity of the tpb at temperatures as low as 70 °C. In the presence of O_2 (P_{O2} = 3.5 kPa), both chemical and electrochemical oxidation of C_2H_4 and CO took place simultaneously, leading to even lower light-off temperatures for both reactions. This effect was also demonstrated for different metal catalysts and supports [116–118].

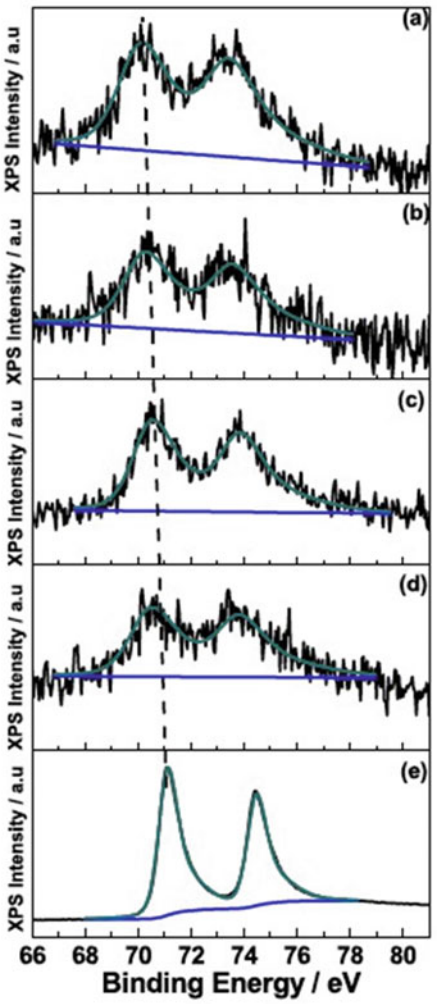

Fig. 3.15 Pt4f XPS peaks of the Pt/YSZ catalysts of various average sizes: (**a**) 1.9 ± 0.4 nm, (**b**) 3.0 ± 0.8 nm, (**c**) 4.4 ± 0.3 nm, (**d**) 6.7 ± 1 nm, (**e**) sputtered Pt foil. (Reprinted with permission from Ref. [114]; Copyright 2014, Elsevier)

An MSI study by Dole et al. [119] investigated the effect of particle size and synthesis parameters on catalytic oxidation of CO. A modified alcohol method was developed that included polyvinylpyrrolidone (PVP) at an optimal PVP/Au ratio of 10:1. Au nanoparticles of 13.1 nm and 17.1 nm supported on YSZ were compared. It was found that calcination is inevitable to remove PVP and achieve activity even though it may increase the particle size. The optimal calcination temperature was based on thermogravimetric analysis (TGA), associated with mass loss of PVP and all species at temperature values of 300 °C and 600 °C, respectively. Higher activity was achieved with lower particle size (13.1 nm), and different calcination temperature did not result in a noticeable change in CO conversion.

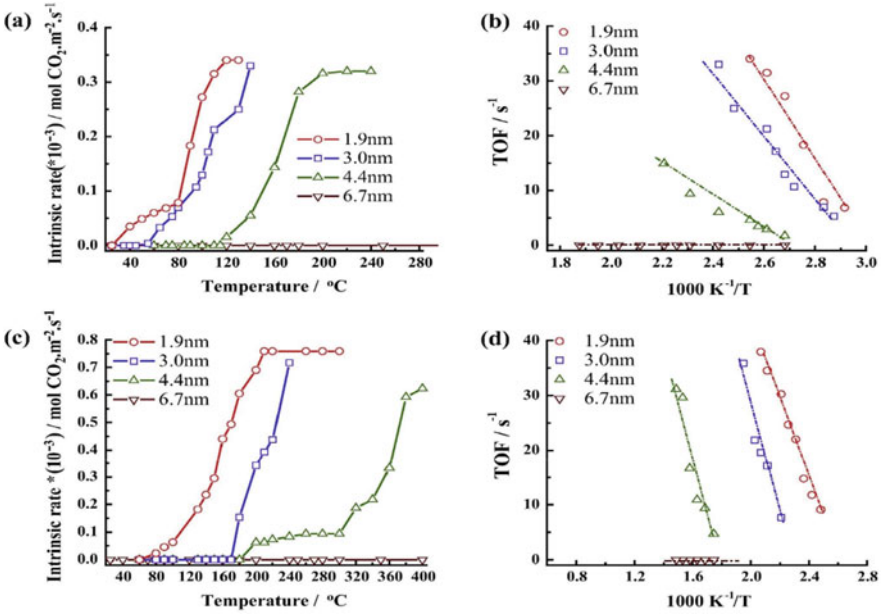

Fig. 3.16 Impact of Pt particle size on YSZ support on the electrooxidation of CO: (**a**) intrinsic rate (normalized with respect to catalyst active surface area), (**b**) turnover frequency, and C_2H_4 electrooxidation (**c**) intrinsic rate (normalized with respect to catalyst active surface area), and (**d**) turnover frequency, both under oxygen-deficient conditions. Flow rate = 77 mL min^{-1}, and concentration reactant = 909 ppm. He balanced. (Reprinted with permission from Ref. [115], Copyright 2015, Elsevier)

The application of electrochemical methods, e.g., cyclic voltammetry, steady-state polarization, chronoamperometry, and chronopotentiometry, has been used in EPOC studies, to in situ characterize, promote, and shed light on the state of the catalyst-working electrode under EPOC conditions. Recently, the use of electrochemical techniques was extended to studying the MSI effect in highly dispersed catalytic systems [117, 120]. The steady-state polarization measurements were carried out to find an exchange current (I_0) of CeO_2-supported Pt- and Ru-based catalysts and link this quantity to the open-circuit catalytic rates. To correlate catalytic and electrochemical measurements, I_0 of each catalyst was obtained from Tafel plots (Fig. 3.18). According to EPOC theory, a good electrocatalyst (high electrochemical reaction rates at the tpb and high I_0) will show an insignificant catalytic rate promotion under polarization because of competing electrochemical reaction and backspillover migration [5, 117]. The following empirical equation was proposed to define an apparent Faradaic efficiency in addition to the fundamental Eq. (3.1) [4]:

$$|\Lambda| \approx \frac{nFr_0}{I_o} \tag{3.4}$$

where r_0 is the open-circuit catalytic rate, I_0 exchange current, n is the number of electrons, and F is Faradic efficiency.

It was found that Eq. (3.4) is also applicable to describe and predict the self-sustained EPOC for the supported and unsupported catalysts in the instance of ethylene oxidation [117]:

$$|\Lambda_{MSI}| \approx \frac{2Fr_0}{I_0} \left(\text{for } O^{2-} \text{ conducting system}\right) \tag{3.5}$$

where $|\Lambda_{MSI}|$ is the self-sustained apparent Faradaic efficiency and other parameters are the same as in Eq. (3.4).

The presence of ceria enhanced the catalytic reaction rate when compared to the free-standing Pt and Ru nanoparticles [117, 120]. The proposed metal-support interaction rate enhancement ratios, ρ_{MSI}, defined as the ratio between the reaction rate of supported NPs over the rate of unsupported (free-standing) NPs was found to be equal to 14. Polarization measurements established that higher exchange current, I_0, values corresponded to the lower open-circuit catalytic rates. The lowest self-induced Faradaic efficiency value ($|\Lambda_{MSI}| = 20$) was for the free-standing Pt nanoparticles, while the highest value ($|\Lambda_{MSI}| = 1053$) corresponded to 1 wt% Pt/CeO_2.

The role of ceria in enhancing the reaction rate created an analogy to the heterojunction phenomenon called the dissimilarity in metal-support work function ($\varphi_{Ru} = 4.71$ eV, $\varphi_{Pt} = 5.93$ eV, $\varphi_{CeO_2} = 4.69$ eV). The difference in work function caused a driving force to transfer O^{2-} from the support (CeO_2) to the metallic catalyst (e.g., Pt, Ru), which is tangible to classical EPOC, where the migration of promoters backspillover under anodic polarization for negative conducting ceramics. The mechanism of self-sustained EPOC and conventional EPOC [5] is illustrated in Fig. 3.17 [118].

The self-induced apparent Faradaic efficiency concept (Eq. 3.5) was further extended to Ni NPs for the complete ethylene oxidation [120]. Ni nanoparticles supported on YSZ and CeO_2 were synthesized using the hydrazine reduction method [121]. The three catalytic systems were free-standing Ni nanoparticles, Ni/CeO_2 (1 wt.% CeO_2), and Ni/YSZ (1 wt.% YSZ). Free-standing Ni NPs, Ni/CeO_2, and Ni/YSZ converted 35%, 43%, and 5% of ethylene at 350 °C, respectively. The apparent Faradic efficiency of MSI (Λ_{MSI}) was calculated based on exchange current density extracted from Tafel plot analysis and revealed that the Λ_{MSI} for Ni/CeO_2 is 2-fold higher than Ni/YSZ. Figure 3.18 shows the summary of catalytic and electrochemical results for several mono- and bimetallic nanoparticles for ethylene oxidation reaction [117, 120]. In all cases, the highest electrochemical rate (high i_0) corresponded to the lowest catalytic rate in agreement with the EPOC backspillover mechanism.

SSEP has been investigated for CO_2 hydrogenation reaction, where commercial Co_3O_4 powder support was used to disperse Ru nanoparticles of ~1 nm average size [62]. Ru NPs were dispersed on Co_3O_4 and deposited on BZY for CO_2 hydrogenation (Fig. 3.19 [16]). Selectivity to CH_4 and CO was 40% and 60%, respectively.

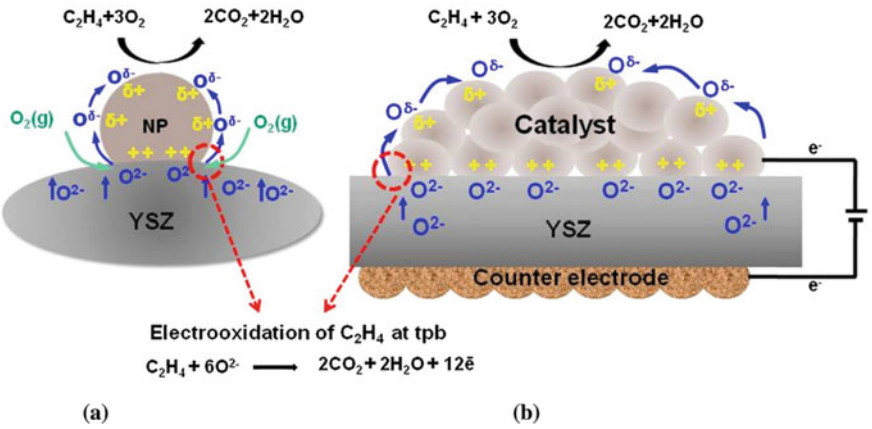

Fig. 3.17 Mechanistic view on processes carrying out over nanoparticles smaller than 5 nm for ethylene oxidation: (**a**) self-sustained EPOC and (**b**) conventional EPOC over electropromoted cell. (Reprinted with permission from Ref. [118]; Copyright 2015, Elsevier)

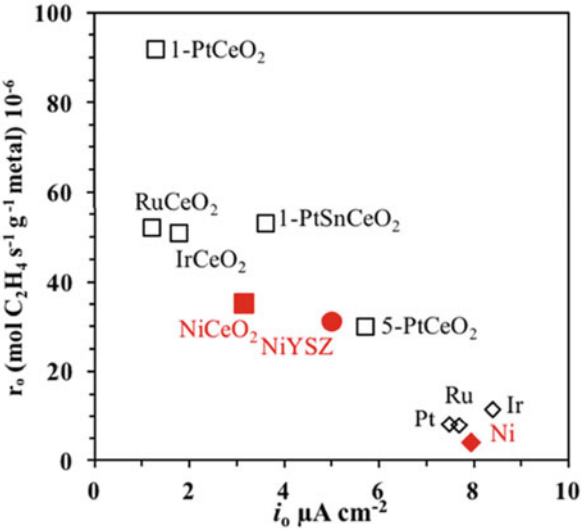

Fig. 3.18 Normalized catalytic rate (r_0) at 350 °C (0.012 kPa C_2H_4, 3 kPa O_2, He balanced) obtained at 350 °C under open-circuit condition and its variation versus exchange current density (i_0). Free-standing Ni, Ni/CeO_2, and 1 wt% Ni/YSZ are shown with red squares. Black symbols correspond to literature results [122, 123]. (Reprinted with permission from Ref. [120]; Copyright 2017, IOP Science)

Under reducing conditions ($CO_2/H_2 = 1:7$), CH_4 selectivity surpassed CO. Only the RWGS reaction was affected under the application of potential following electrophilic behavior where the CO rate decreased under positive polarization and increased during negative polarization. The spontaneous migration of H^+ from BZY aided in reducing Co_3O_4 to cycle oxygen by creating vacancies. Above 350 °C, Co_3O_4 conducted protons from BZY and electrons onto the Ru nanoparticles. The change in catalytic rate was minimally affected by ~10%, where it was suggested that Ru/Co_3O_4 was already in a promoted state or SSEP.

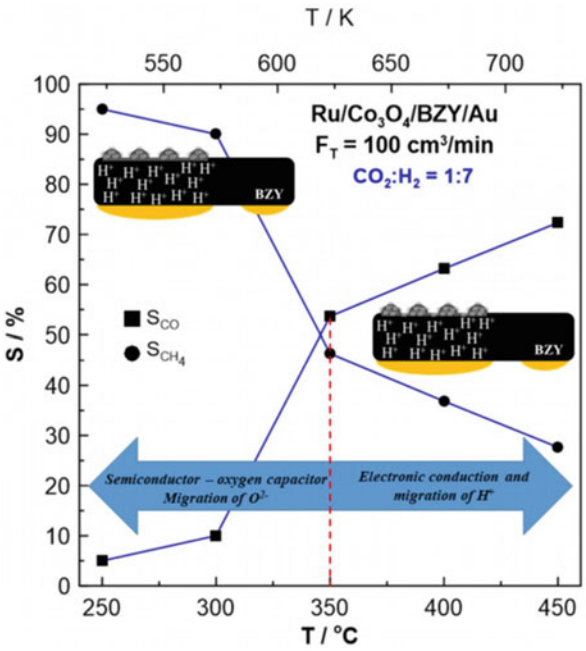

Fig. 3.19 Electrochemical activity of Ru/Co_3O_4 as a function of temperature. Under 350 °C Co_3O_4 cycles oxygen with Ru and the reactants, above 350 °C H^+ ions from BZY migrate on the Ru/Co_3O_4. (Reprinted with permission from Ref. [16]; Copyright 2020, Elsevier)

The ability of Co_3O_4 to act as a conduit of protons and electrons replaces the need to employ a conductive film to polarize the catalyst as shown in the Ru-Co nanoparticles deposited on the Ru intermediate film [63].

Panaritis *et al.* [124] carried out an electrochemical study of FeO_x nanowires dispersed on Co_3O_4 commercial powder support for RWGS. The authors found that Co_3O_4 influenced the morphology of FeO_x nanowires. When FeO_x was dispersed on Co_3O_4, the morphology of the nanowires (length ~100–500 nm, diameter ~5 nm) changed to spherical particles of 5 nm. Under open-circuit conditions, FeO_x/Co_3O_4 outperformed FeO_x/Al_2O_3 by 20 times. Under anodic and cathodic polarization, the CO rate decreased by 10% (or $\rho = 0.9$) or referred to as volcano behavior. Polarization led to the suppression in the catalytic rate of FeO_x/Co_3O_4 by altering the oxidation state of Co_3O_4 and as a result its MSI effect with FeO_x. Electrochemical polarization was used as a tool to study the MSI or SSEP effect between FeO_x and Co_3O_4. Thus, under polarization, the active state of FeO_x/Co_3O_4 is hindered suggesting that the catalyst is in an SSEP state under reaction conditions.

Another interesting aspect of promotion termed electric field promotion has been reported in recent years [125–133]. In [127, 128], the authors proposed a mechanism of ultra-lean methane oxidation over different Pd-Ce-Zr catalysts in a fixed-bed reactor under 0.2% CH_4 mixed with 10% O_2 and N_2 balance. The catalytic reactor consisted of two stainless steel electrodes positioned with no gap (Fig. 3.20). The product analysis was carried out by FTIR spectroscopy, and the increase in turnover frequency (under direct electric field) was normalized based on consumed power per

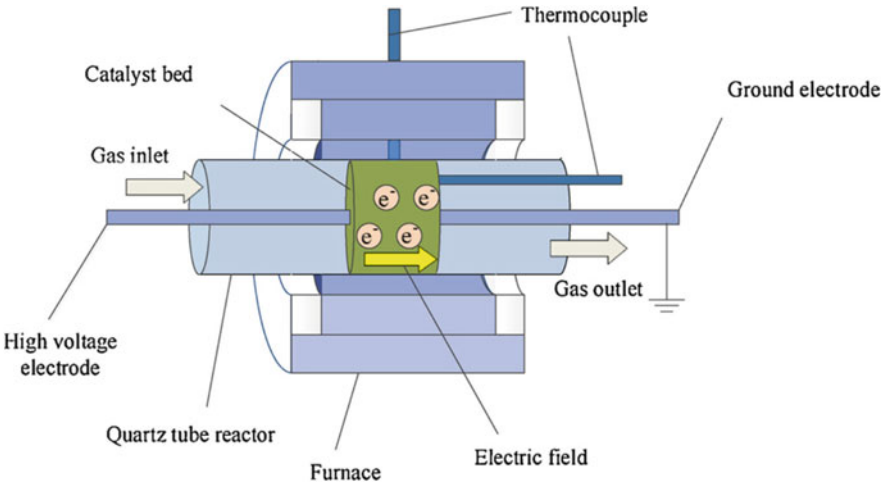

Fig. 3.20 Schematic representation of experimental setup design combining the catalytic process with an electric field. (Reprinted with permission from Ref. [125]; Copyright 2018, Elsevier)

run referred to as ΔTOF^{*} [$s^{-1}w^{-1}$]. The decrease in the light-off temperature and increase in ΔTOF^{*} was due to an electric field that resulted in the release of lattice oxygen ions present in the support. Thus, more surface localized oxygen was produced to oxidize Pd^{0}. This in turn promoted the dissociative chemisorption of CH_4 and its subsequent dehydrogenation while eliminating formate intermediates. Therefore, carbonates were directly formed through CH species. In addition, the reducibility of PdO_x was favorably altered via an electric field, which led to CH_4 oxidation at a lower temperature. Other examples of electric field promotion include oxidation of benzene [129, 130], toluene [131], naphthalene[132], and lean methane combustion over Mn_xCo_y [133].

3.4 Conclusion and Prospective Research Gaps

This chapter provides an overview of recent advances in EPOC of nanostructured catalysis covering both classical and self-sustained EPOC. The last two decades witnessed a large growth in the use of highly dispersed, nano-sized catalytic systems in electrochemical promotion studies. Furthermore, these studies confirmed the functional similarity between EPOC and MSI when ionically conductive ceramics are used as active supports, and the mechanism involved in both phenomena has been further elucidated. As we demonstrate in this review, the nanoparticle catalytic systems could be efficiently electropromoted for reforming, oxidation, and hydrogenation reactions. The application of various synthesis procedures (sputtering, PVD, ALD, impregnation, polyol, and hydrazine reduction methods) led to the

fabrication of mono- and bimetallic catalysts of well-defined size, composition, as well as bulk and surface structure. Furthermore, theoretical calculations based on DFT were discussed for Pt(111), RuO_2(110), and Ru(0001) surfaces that closely model the real nanoparticle systems. Despite tremendous progress in EPOC with noble (Pt, Pd, Rh, Au, etc.) and especially with non-noble (Fe, Co, Cu, Ni) metal and metal oxide nanoparticles, there are still several research gaps that need to be addressed for the future advancement of EPOC with a goal of developing and fabricating active and stable catalytic systems:

1. Further Development and Application of In Situ and Operando Techniques for EPOC and MSI Investigation

Additional experimental in situ observations of EPOC are still needed. Diffuse reflectance infrared Fourier transform spectroscopy (DRIFTS) is an informative technique to in situ analyze reaction mechanisms for the highly dispersed powder catalysts commonly used in MSI studies. This technique requires highly dispersed powder samples and shows limitations for studying thin films due to their low surface area and dispersion. Instead, the polarization modulation infrared reflection absorption spectroscopy (PM-IRRAS) technique could be employed to study the electrode surfaces of thin films for EPOC applications [134, 135]. Urakawa et al. demonstrated how the surface species change on the surface of a Pt thin film (40 nm) during CO oxidation using PM-IRRAS. With a modification in the reactor design and configuration, the same film can be studied under polarization with solid electrolyte support. In situ XPS measurements are useful to identify the change in the oxidation state of the catalyst-working electrode as a function of applied potential and differentiate between electrochemically induced $O^{\delta-}$ on the surface over chemisorbed atomic oxygen [70]. Both in situ approaches require specific reactor configurations that ensure electrochemical conductivity between the electrodes and high temperature to ensure ionic conductivity from the solid electrolyte to promote the catalyst-working electrode. Other important techniques like in situ X-ray absorption spectroscopy (XAS) and various electron microscopies could further shed light on the EPOC phenomenon.

2. Cell Design for Efficient NP Polarization

As discussed throughout this chapter, the use of nanoparticles as a catalyst-working electrode has clear advantages over the micrometer-thick, continuous film electrodes. However, when moving from a uniform porous, thick metal or metal oxide film, where one point of contact with the electrode is enough to ensure conductivity, to NPs, novel cell designs and current collectors are required. For nanostructured electrodes, composed of non-percolated single NPs or NPs islands, there are many challenges in assuring the conductivity and the uniform current distribution. New current collector design and electrode configurations are needed. The inert current collector in the form of a mesh, rings, or any other pattern could be deposited over the catalyst. Other approaches could include an inert, conductive interlayer between the solid electrolyte and catalytic NPs. The application of bipolar and wireless EPOC configurations is very promising in this regard. For instance,

researchers designed different current collectors: (i) direct polarization, e.g., using a gold mesh [17, 48, 112], and (ii) sputtering catalyst on the conductive support [8, 115, 118, 136]. As one of the recent advances in sputtering techniques, Vernoux's group [136] designed a current collector inspired from fuel cell technology for SS-EPOC of NO_x storage-reduction reactions (see Fig. 2.21 in Chap. 2). This current collector was prepared by dispersing Pt and Rh NPs on YSZ (acting as nanometric electrodes). Then, Pt/Rh/YSZ catalytic systems (in the form of a powder) were deposited in the location of the porous structure of the SiC diesel particulate filter (DPFs). DPFs can play the role of the external circuit to transport electrons between nanoparticles and, in the case of being doped with N, enhance their electronic conductivity. Two scenarios of using Pt/Rh/YSZ over N-doped SiC and un-doped SiC were studied under cycling conditions (lean/rich). The following observations were reported: (i) overproduction of CO_2 under rich cycle (absence of oxygen) explained by CO electrochemical reaction [8, 115, 118], (ii) N-doped SiC displayed the highest catalytic activity, and (iii) O^{2-} backspillover (from YSZ onto the surface of Pt) with NPs smaller than 5 nm while >10 nm required the existence of electromotive force (EMF). Such EMF can be induced via two distinct metals and a conductor with sufficient electronic conductivity.

Furthermore, the wireless electrochemical promotion has a great potential for practical application of the EPOC phenomenon. Stavrakakis et al. [137] studied wireless EPOC on modified catalytic membrane reactors employing $BaCe_{1-x}Y_xO_{3-\delta}$ (BCY) and $BaCe_{0.8-y}\ Zr_yY_{0.2}\ O_{3-\delta}$ (BCZY) conductive membrane supports. In this study, wireless EPOC configuration [138–143] utilized the chemical potential difference between the dense membrane support with a Pt film (synthesized via sol-gel method) painted on both sides of BCZY disk (Fig. 3.21). Catalytic CO oxidation was carried out with a total flow rate of 200 mL min^{-1} and partial pressure of 1 kPa and 10 kPa for CO and O_2, respectively, where the high partial pressure for oxygen was selected to prevent carbon deposition and subsequent poisoning. In addition, H_2/H_2O flowing through the sweep side of a dual-chamber reactor supplied promoters to the catalyst and reaction side. The best performance was obtained by BCZ20Y20 where a 10% promotion reaction rate was reported at 650 °C with a reversible EPOC behavior and tenable membrane stability. The barrier is to explain the suppressed promotion in subsequent H_2/H_2O and Ar sweep cycles in which the former sweep generated an H_2 chemical potential gradient from sweep to reaction side and emerged the ambipolar diffusion of H^+ (proton) and $O^{\delta-}$ ions. In the second and third cycles, the promotion is completely suppressed as two conducting (or competing) mechanisms: (i) hydrogen chemical potential gradient and (ii) ambipolar diffusion of proton and oxygen ions might reach an equilibrium.

Using Pt NPs instead of a Pt film might shift the competing mechanism in a favorable way to obtain the desirable flux of $O^{\delta-}$ and H^+ ions to carry out promotion through subsequent cycles (the second and third one). This possible anticipation of NPs may preserve sustainable and stable CO oxidation. In addition, using BCZY as a solid electrolyte in other types of EPOC reactions may exhibit positive enhancement with respect to activation and reaction temperature, stability, and promotion.

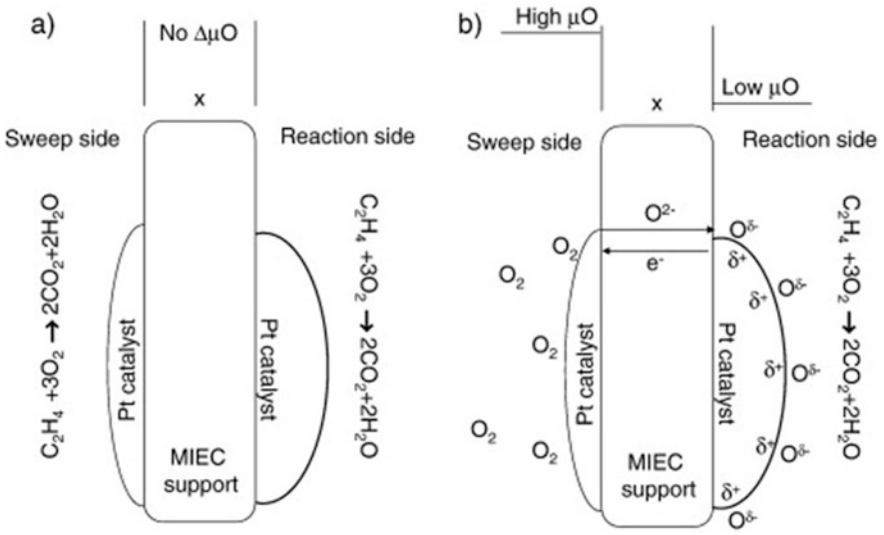

Fig. 3.21 Operation and promotional mechanism of wireless EPOC configuration: (**a**) symmetrical operation and (**b**) O_2 sweep. (Reprinted with permission from Ref. [142]; Copyright 2008, Elsevier)

3. Development of Catalytic Systems Without Noble Metal Content or with Reduced Noble Metal Content

Various nanostructured catalytic systems (non-noble or with reduced metal content) have been studied for EPOC reactions over the last 10 years for complete methane oxidation over Ni9Pd [54]; RWGS reactions over Co [93], FeO_x [17], $RuFeO_x$ [92], and Cu; WGR over Ni[91]; CO_2 hydrogenation over Ni [88] and Cu [84]; and partial oxidation of methanol over Cu[83]. Further development and implementation of nanostructured bimetallic and ternary catalysts for EPOC of other environmentally and technologically important reactions are needed.

4. Development and Application of Novel Conducting Ceramics and Polymers as Solid Electrolytes

Yttria-stabilized zirconia is the most used solid electrolyte in EPOC studies to date. YSZ requires high temperatures of at least of 280 °C to have an observable bulk ionic conductivity [5]. In addition to low ionic conductivity, YSZ is quite expensive: 0.56 USD g^{-1} [144, 145]. In laboratory experiments, a relatively thick (several mm) YSZ disk is used as a solid electrolyte, which has limitations for a scale-up application. A recent study attempted to synthesize thin-film NEMCA cells on conventional alumina supports with and without $BiCuVO_x$ [146]. Another direction is the development of novel solid-state electrolytes that display high ionic conductivity at lower temperatures with high chemical and mechanical stability. This could reduce the temperature required for ionic conductivity and extend EPOC to a wide range of low-temperature reactions and systems.

References

1. Stoukides M, Vayenas CG (1981) The effect of electrochemical oxygen pumping on the rate and selectivity of ethylene oxidation on polycrystalline silver. J Catal 70:137–146. https://doi.org/10.1016/0021-9517(81)90323-7
2. Bebelis S, Vayanes CG (1989) Non-faradaic electrochemical modification of catalytic activity 1. The case of ethylene oxidation on Pt. J Catal 118:125–146. https://doi.org/10.1016/0021-9517(89)90306-0
3. Vayanes CG, Bebelis S (1999) Electrochemical promotion of heterogeneous catalysis. Catal Today 51:581–594. https://doi.org/10.1016/S0920-5861(99)00042-5
4. Vayenas CG, Bebelis S, Pliangos C, Brosda S (2001) Electrochemical activation of catalysis promotion, electrochemical promotion, and metal-support interactions. Kluwer Academic Publishers
5. Vernoux P, Lizarraga L, Tsampas MN, Sapountzi FM, De Lucas-Consuegra A, Valverde JL, Souentie S, Vayenas CG, Tsiplakides D, Balomenou S, Baranova EA (2013) Ionically conducting ceramics as active catalyst supports. Chem Rev 113:8192–8260. https://doi.org/10.1021/cr4000336
6. Urquhart AJ, Williams FJ, Lambert RM (2005) Electrochemical promotion by potassium of Rh-catalysed fischer-tropsch synthesis at high pressure. Catal Lett 103:137–141. https://doi.org/10.1007/s10562-005-6519-1
7. Panaritis C, Edake M, Couillard M, Einakchi R, Baranova EA (2018) Insight towards the role of ceria-based supports for reverse water gas shift reaction over RuFe nanoparticles. J CO2 Util 26:350–358. https://doi.org/10.1016/j.jcou.2018.05.024
8. Isaifan RJ, Baranova EA (2013) Catalytic electrooxidation of volatile organic compounds by oxygen-ion conducting ceramics in oxygen-free gas environment. Electrochem Commun 27:164–167. https://doi.org/10.1016/j.elecom.2012.11.021
9. Kalaitzidou I, Zagoraios D, Brosda S, Katsaounis A, Vernoux P, Vayenas CG (2018) Electrochemical promotion of methane oxidation on Pd nanoparticles deposited on YSZ. Mater Today Proc 5:27345–27352. https://doi.org/10.1016/J.MATPR.2018.09.050
10. Jiménez-Borja C, Dorado F, de Lucas-Consuegra A, Vargas JMG, Valverde JL (2011) Electrochemical promotion of CH4 combustion over a Pd/CeO2–YSZ catalyst. Fuel Cells 11:131–139. https://doi.org/10.1002/fuce.201000058
11. Nakos A, Souentie S, Katsaounis A (2010) Electrochemical promotion of methane oxidation on Rh/YSZ. Appl Catal B Environ 101:31–37. https://doi.org/10.1016/J.APCATB.2010.08.030
12. López ER, Dorado F, de Lucas-Consuegra A (2019) Electrochemical promotion for hydrogen production via ethanol steam reforming reaction. Appl Catal B Environ 243:355–364. https://doi.org/10.1016/j.apcatb.2018.10.062
13. De Lucas-Consuegra A, González-Cobos J, Carcelén V, Magén C, Endrino JL, Valverde JL (2013) Electrochemical promotion of Pt nanoparticles dispersed on a diamond-like carbon matrix: a novel electrocatalytic system for H2 production. J Catal 307:18–26. https://doi.org/10.1016/j.jcat.2013.06.012
14. Vernoux P (2017) Recent advances in electrochemical promotion of catalysis. Catalysis 29:29–59. https://doi.org/10.1039/9781788010634-00029
15. Jiménez V, Jiménez-Borja C, Sánchez P, Romero A, Papaioannou EI, Theleritis D, Souentie S, Brosda S, Valverde JL (2011) Electrochemical promotion of the CO2 hydrogenation reaction on composite ni or ru impregnated carbon nanofiber catalyst-electrodes deposited on YSZ. Appl Catal B Environ 107:210–220. https://doi.org/10.1016/j.apcatb.2011.07.016
16. Zagoraios D, Panaritis C, Krassakopoulou A, Baranova EA, Katsaounis A, Vayenas CG (2020) Electrochemical promotion of Ru nanoparticles deposited on a proton conductor electrolyte during CO2 hydrogenation. Appl Catal B Environ 276:119148. https://doi.org/10.1016/j.apcatb.2020.119148

17. Panaritis C, Zgheib J, Ebrahim SAH, Couillard M, Baranova EA (2020) Electrochemical in-situ activation of Fe-oxide nanowires for the reverse water gas shift reaction. Appl Catal B Environ 269:118826. https://doi.org/10.1016/j.apcatb.2020.118826
18. Fellah Jahromi A, Ruiz-López E, Dorado F, Baranova EA, de Lucas-Consuegra A (2022) Electrochemical promotion of ethanol partial oxidation and reforming reactions for hydrogen production. Renew Energy 183:515–523. https://doi.org/10.1016/J.RENENE.2021.11.041
19. Shim JH, Park JS, Holme TP, Crabb K, Lee W, Kim YB, Tian X, Gür TM, Prinz FB (2012) Enhanced oxygen exchange and incorporation at surface grain boundaries on an oxide ion conductor. Acta Mater 60:1–7. https://doi.org/10.1016/J.ACTAMAT.2011.09.050
20. Siebert E, Djurado E, Pagnier T, Roux C, Vernoux P (2005) In-situ high temperature study of oxygen adsorbed on Pt/YSZ under conditions of electrochemical promotion of catalysis. In: Risoe international symposium on materials science. Roskilde
21. Skriver HL, Rosengaard NM (1992) Surface energy and work function of elemental metals. Phys Rev B 46:7157–7168. https://doi.org/10.1103/PhysRevB.46.7157
22. Vayenas CG, Brosda S (2014) Electron donation-Backdonation and the rules of catalytic promotion. Top Catal 57:1287–1301. https://doi.org/10.1007/s11244-014-0294-4
23. Vayenas CG, Brosda S, Pliangos C (2001) Rules and mathematical modeling of electrochemical and chemical promotion: 1. Reaction classification and promotional rules. J Catal 203: 329–350. https://doi.org/10.1006/jcat.2001.3348
24. Brosda S, Vayenas CG (2002) Rules and mathematical modeling of electrochemical and classical promotion: 2. Modeling. J Catal 208:38–53. https://doi.org/10.1006/jcat.2002.3549
25. Brosda S, Vayenas CG, Wei J (2006) Rules of chemical promotion. Appl Catal B Environ 68: 109–124. https://doi.org/10.1016/j.apcatb.2006.07.021
26. Nicole J, Tsiplakides D, Wodiunig S, Comninellis C (1997) Activation of catalyst for gas-phase combustion by electrochemical pretreatment. J Electrochem Soc 144. https://doi.org/10.1149/1.1838143
27. González-Cobos J, de Lucas-Consuegra A (2016) A review of surface analysis techniques for the investigation of the phenomenon of electrochemical promotion of catalysis with alkaline ionic conductors. Catalysts 6. https://doi.org/10.3390/catal6010015
28. Yentekakis IV, Vernoux P, Goula G, Caravaca A (2019) Electropositive promotion by alkalis or alkaline earths of Pt-group metals in emissions control catalysis: a status report. Catalysts 9: 157. https://doi.org/10.3390/catal9020157
29. Katsaounis A (2009) Recent developments and trends in the electrochemical promotion of catalysis (EPOC). J Appl Electrochem 405(40):885–902. https://doi.org/10.1007/S10800-009-9938-7
30. Isaifan RJ, Dole HAE, Obeid E, Lizarraga L, Vernoux P, Baranova EA (2012) Metal-support interaction of Pt nanoparticles with ionically and non-ionically conductive supports for CO oxidation. Electrochem Solid-State Lett 15:E14. https://doi.org/10.1149/2.024203esl
31. Xia C, Hugentobler M, Li Y, Foti G, Comninellis C, Harbich W (2011) Electrochemical promotion of CO combustion over non-percolated Pt particles supported on YSZ using a novel bipolar configuration. Electrochem Commun 13:99–101. https://doi.org/10.1016/j.elecom.2010.11.026
32. Marwood M, Vayenas CG (1998) Electrochemical promotion of a dispersed platinum catalyst. J Catal 178:429–440. https://doi.org/10.1006/jcat.1998.2156
33. Vernoux P, Gaillard F, Bultel L, Siebert E, Primet M (2002) Electrochemical promotion of propane and propene oxidation on Pt/YSZ. J Catal 208. https://doi.org/10.1006/jcat.2002.3573
34. Dole HAE, Isaifan RJ, Sapountzi FM, Lizarraga L, Aubert D, Princivalle A, Vernoux P, Baranova EA (2013) Low temperature toluene oxidation over Pt nanoparticles supported on yttria stabilized-zirconia. Catal Lett 143:996–1002. https://doi.org/10.1007/s10562-013-1071-x
35. Souentie S, Lizarraga L, Kambolis A, Alves-Fortunato M, Valverde JL, Vernoux P (2011) Electrochemical promotion of the water-gas shift reaction on Pt/YSZ. J Catal 283:124–132. https://doi.org/10.1016/j.jcat.2011.07.009

36. Palma V, Ruocco C, Cortese M, Renda S, Meloni E, Festa G, Martino M (2020) Platinum based catalysts in the water gas shift reaction: recent advances. Metals (Basel) 10:1–74. https://doi.org/10.3390/met10070866
37. Roche V, Revel R, Vernoux P (2010) Electrochemical promotion of YSZ monolith honeycomb for deep oxidation of methane. Catal Commun 11. https://doi.org/10.1016/j.catcom.2010.05.005
38. De Lucas-Consuegra A, Caravaca A, Martínez PJ, Endrino JL, Dorado F, Valverde JL (2010) Development of a new electrochemical catalyst with an electrochemically assisted regeneration ability for H2 production at low temperatures. J Catal 274:251–258. https://doi.org/10.1016/j.jcat.2010.07.007
39. Xia C, Hugentobler M, Yongdan-Li CC, Harbich W (2010) Quantifying electrochemical promotion of induced bipolar Pt particles supported on YSZ. Electrochem Commun 12:1551–1554. https://doi.org/10.1016/j.elecom.2010.08.031
40. Falgairette C, Xia C, Li Y, Harbich W, Foti G, Comninellis C (2010) Investigation of the Pt/YSZ interface at low oxygen partial pressure by solid electrochemical mass spectroscopy under high vacuum conditions. J Appl Electrochem 4010(40):1901–1907. https://doi.org/10.1007/S10800-010-0160-4
41. Jaccoud A, Falgairette C, Fóti G, Comninellis C (2007) Charge storage in the O2(g),Pt/YSZ system. Electrochim Acta 52:7927–7935. doi: https://doi.org/10.1016/j.electacta.2007.06.046
42. Kambolis A, Lizarraga L, Tsampas MN, Burel L, Rieu M, Viricelle J-P, Vernoux P (2012) Electrochemical promotion of catalysis with highly dispersed Pt nanoparticles. Electrochem Commun:19. https://doi.org/10.1016/j.elecom.2012.02.041
43. Li X, Gaillard F, Vernoux P (2005) The relationship of the catalytic activity and the open-circuit potential of Pt interfaced with YSZ. Ionics 111(11):103–111. https://doi.org/10.1007/BF02430408
44. Fortunato MA, Princivalle A, Capdeillayre C, Petigny N, Tardivat C, Guizard C, Tsampas MN, Sapountzi FM, Vernoux P (2014) Role of lattice oxygen in the propane combustion over Pt/Yttria-stabilized zirconia: isotopic studies. Top Catal 57:1277–1286. https://doi.org/10.1007/s11244-014-0293-5
45. De Lucas-Consuegra A, González-Cobos J, García-Rodríguez Y, Mosquera A, Endrino JL, Valverde JL (2012) Enhancing the catalytic activity and selectivity of the partial oxidation of methanol by electrochemical promotion. J Catal 293:149–157. https://doi.org/10.1016/j.jcat.2012.06.016
46. De Lucas-Consuegra A, González-Cobos J, Gacia-Rodriguez Y, Endrino JL, Valverde JL (2012) Electrochemical activation of the catalytic methanol reforming reaction for H 2 production. Electrochem Commun 19:55–58. https://doi.org/10.1016/j.elecom.2012.03.016
47. Hajar Y, Di Palma V, Kyriakou V, Verheijen MA, Baranova EA, Vernoux P, Kessels WMM, Creatore M, van de Sanden MCM, Tsampas M (2017) Atomic layer deposition of highly dispersed Pt nanoparticles on a high surface area electrode backbone for electrochemical promotion of catalysis. Electrochem Commun:84. https://doi.org/10.1016/j.elecom.2017.09.023
48. Hajar YM, Patel KD, Tariq U, Baranova EA (2017) Functional equivalence of electrochemical promotion and metal support interaction for Pt and RuO2 nanoparticles. J Catal 352:42–51. https://doi.org/10.1016/j.jcat.2017.05.001
49. Baranova EA, Bock C, Ilin D, Wang D, MacDougall B (2006) Infrared spectroscopy on size-controlled synthesized Pt-based nano-catalysts. Surf Sci 600:3502–3511. https://doi.org/10.1016/j.susc.2006.07.005
50. Yeung KL, Christiansen SC, Varma A (1999) Palladium composite membranes by electroless plating technique: relationships between plating kinetics, film microstructure and membrane performance. J Memb Sci 159:107–122. https://doi.org/10.1016/S0376-7388(99)00041-1
51. Matei F, Jiménez-Borja C, Canales-Vázquez J, Brosda S, Dorado F, Valverde JL, Ciuparu D (2013) Enhanced electropromotion of methane combustion on palladium catalysts deposited on highly porous supports. Appl Catal B Environ 132–133:80–89. https://doi.org/10.1016/j.apcatb.2012.11.011

52. Zagoraios D, Athanasiadi A, Kalaitzidou I, Ntais S, Katsaounis A, Caravaca A, Vernoux P, Vayenas CG (2020) Electrochemical promotion of methane oxidation over nanodispersed Pd/Co3O4 catalysts. Catal Today 355:910–920. https://doi.org/10.1016/J.CATTOD.2019.02.030
53. Hajar YM, Venkatesh B, Baranova EA (2019) Electrochemical promotion of nanostructured palladium catalyst for complete methane oxidation. Catalysts 9:48. https://doi.org/10.3390/catal9010048
54. Hajar YM, Venkatesh B, Houache MSE, Liu H, Safari R, Prabhudev S, Botton GA, Baranova EA (2019) Electrochemical promotion of Bi-metallic Ni9Pd core double-shell nanoparticles for complete methane oxidation. J Catal 374:127–135. https://doi.org/10.1016/j.jcat.2019.04.026
55. Chang Q, Xu Y, Duan Z, Xiao F, Fu F, Hong Y, Kim J, Choi S-I, Su D, Shao M (2017) Structural evolution of Sub-10 nm octahedral platinum–nickel bimetallic nanocrystals. Nano Lett 17:3926–3931. https://doi.org/10.1021/ACS.NANOLETT.7B01510
56. Bebelis S, Karasali H, Vayenas CG (2008) Electrochemical promotion of the CO2 hydrogenation on Pd/YSZ and Pd/β″-Al2O3 catalyst-electrodes. Solid State Ionics 179:1391–1395. https://doi.org/10.1016/j.ssi.2008.02.043
57. Cai F, Gao D, Zhou H, Wang G, He T, Gong H, Miao S, Yang F, Wang J, Bao X (2017) Electrochemical promotion of catalysis over Pd nanoparticles for CO2 reduction. Chem Sci 8:2569–2573. https://doi.org/10.1039/c6sc04966d
58. Solymosi F, Erdöhelyi A (1980) Hydrogenation of CO2 to CH4 over alumina-supported noble metals. J Mol Catal 8:471–474. https://doi.org/10.1016/0304-5102(80)80086-1
59. Ryu J, Surendranath Y (2020) Polarization-induced local pH swing promotes Pd-catalyzed CO2 hydrogenation. J Am Chem Soc 142:13384–13390. https://doi.org/10.1021/jacs.0c01123
60. Fuel Cell Store (2020) Fuel cell store
61. Hajar YM, Treps L, Michel C, Baranova EA, Steinmann SN (2019) Theoretical insight into the origin of the electrochemical promotion of ethylene oxidation on ruthenium oxide. Cat Sci Technol 9:5915–5926. https://doi.org/10.1039/c9cy01421g
62. Panaritis C, Michel C, Couillard M, Baranova EA, Steinmann SN (2020) Elucidating the role of electrochemical polarization on the selectivity of the CO2 hydrogenation reaction over Ru. Electrochim Acta 350:136405. https://doi.org/10.1016/j.electacta.2020.136405
63. Kotsiras A, Kalaitzidou I, Grigoriou D, Symillidis A, Makri M, Katsaounis A, Vayenas CG (2018) Electrochemical promotion of nanodispersed Ru-Co catalysts for the hydrogenation of CO2. Appl Catal B Environ 232:60–68. https://doi.org/10.1016/j.apcatb.2018.03.031
64. Theleritis D, Souentie S, Siokou A, Katsaounis A, Vayenas CG (2012) Hydrogenation of CO2 over Ru/YSZ Electropromoted catalysts. ACS Catal 2:770–780. https://doi.org/10.1021/CS300072A
65. Theleritis D, Makri M, Souentie S, Caravaca A, Katsaounis A, Vayenas CG (2014) Comparative study of the electrochemical promotion of CO2 hydrogenation over Ru-supported catalysts using electronegative and electropositive promoters. ChemElectroChem 1:254–262. https://doi.org/10.1002/CELC.201300185
66. Kalaitzidou I, Makri M, Theleritis D, Katsaounis A, Vayenas CG (2016) Comparative study of the electrochemical promotion of CO2 hydrogenation on Ru using Na+, K+, H+ and O2- conducting solid electrolytes. Surf Sci 646:194–203. https://doi.org/10.1016/j.susc.2015.09.011
67. Baranova EA, Thursfield A, Brosda S, Fóti G, Comninellis C, Vayenas CG (2005) Electrochemical promotion of ethylene oxidation over Rh catalyst thin films sputtered on YSZ and TiO[sub 2]/YSZ supports. J Electrochem Soc 152:E40. https://doi.org/10.1149/1.1839511
68. Baranova EA, Thursfield A, Brosda S, Fóti G, Comninellis C, Vayenas CG (2005) Electrochemically induced oscillations of C2H4 oxidation over thin sputtered Rh catalyst films. Catal Lett 1051(105):15–21. https://doi.org/10.1007/S10562-005-7999-8

69. Pliangos C, Yentekakis IV, Verykios XE, Vayenas CG (1995) Non-faradaic electrochemical modification of catalytic activity: VIII. Rh-catalyzed C2H4 oxidation. J Catal 154:124–136. https://doi.org/10.1006/JCAT.1995.1154
70. Katsaounis A, Teschner D, Zafeiratos S (2018) The effect of polarization and reaction mixture on the Rh/YSZ oxidation state during ethylene oxidation studied by near ambient pressure XPS. Top Catal 61:2142–2151. https://doi.org/10.1007/s11244-018-1073-4
71. Katsaounis A, Nikopoulou Z, Verykios XE, Vayenas CG (2004) Comparative isotope-aided investigation of electrochemical promotion and metal–support interactions: 2. CO oxidation by 18O2 on electropromoted Pt films deposited on YSZ and on nanodispersed Pt/YSZ catalysts. J Catal 226:197–209. https://doi.org/10.1016/J.JCAT.2004.05.009
72. Vayenas CG, Koutsodontis CG (2008) Non-faradaic electrochemical activation of catalysis. J Chem Phys 128:182506. https://doi.org/10.1063/1.2824944
73. Kishi K, Daté M, Haruta M (2001) Effect of gold on the oxidation of the Si(1 1 1)-7×7 surface. Surf Sci 486:L475–L479. https://doi.org/10.1016/S0039-6028(01)01083-4
74. Haruta M (2003) When gold is not noble: catalysis by nanoparticles. Chem Rec 3:75–87. https://doi.org/10.1002/TCR.10053
75. Haruta M (2004) Gold as a novel catalyst in the 21st century: preparation, working mechanism and applications. ChemInform 35. https://doi.org/10.1002/CHIN.200444247
76. González-Cobos J, Horwat D, Ghanbaja J, Valverde JL, De Lucas-Consuegra A (2014) Electrochemical activation of Au nanoparticles for the selective partial oxidation of methanol. J Catal 317:293–302. https://doi.org/10.1016/j.jcat.2014.06.022
77. Pestryakov AN, Lunin VV, Bogdanchikova N, Temkin ON, Smolentseva E (2013) Active states of gold in small and big metal particles in CO and methanol selective oxidation. Fuel 110:48–53. https://doi.org/10.1016/J.FUEL.2012.10.012
78. Chang FW, Lai SC, Roselin LS (2008) Hydrogen production by partial oxidation of methanol over ZnO-promoted Au/Al2O3 catalysts. J Mol Catal A Chem 282:129–135. https://doi.org/10.1016/J.MOLCATA.2007.12.002
79. Kähler K, Holz MC, Rohe M, Van Veen AC, Muhler M (2013) Methanol oxidation as probe reaction for active sites in Au/ZnO and Au/TiO2 catalysts. J Catal 299:162–170. https://doi.org/10.1016/J.JCAT.2012.12.001
80. Cavoué T, Caravaca A, Kalaitzidou I, Gaillard F, Rieu M, Viricelle JP, Vernoux P (2019) Ethylene epoxidation on Ag/YSZ electrochemical catalysts: understanding of oxygen electrode reactions. Electrochem Commun 105:106495. https://doi.org/10.1016/j.elecom.2019.106495
81. Fee M, Ntais S, Weck A, Baranova EA (2014) Electrochemical behavior of silver thin films interfaced with yttria-stabilized zirconia. J Solid State Electrochem 188(18):2267–2277. https://doi.org/10.1007/S10008-014-2477-0
82. Kalaitzidou I, Cavoué T, Boreave A, Burel L, Gaillard F, Retailleau-Mevel L, Baranova EA, Rieu M, Viricelle JP, Horwat D, Vernoux P (2018) Electrochemical promotion of propylene combustion on Ag catalytic coatings. Catal Commun 104:28–31. https://doi.org/10.1016/j.catcom.2017.10.005
83. González-Cobos J, Rico VJ, González-Elipe AR, Valverde JL, De Lucas-Consuegra A (2015) Electrochemical activation of an oblique angle deposited Cu catalyst film for H2 production. Cat Sci Technol 5:2203–2214. https://doi.org/10.1039/c4cy01524j
84. Ruiz E, Cillero D, Martínez PJ, Morales Á, Vicente GS, De Diego G, Sánchez JM (2014) Electrochemical synthesis of fuels by CO2 hydrogenation on Cu in a potassium ion conducting membrane reactor at bench scale. Catal Today 236:108–120. https://doi.org/10.1016/j.cattod.2014.01.016
85. Wang J, Couillard M, Baranova E (2022) Electrochemical promotion of copper nanoparticles for the reverse water gas shift reaction. Cat Sci Technol. https://doi.org/10.1039/D1CY02315B

86. Persson K, Ersson A, Colussi S, Trovarelli A, Järås SG (2006) Catalytic combustion of methane over bimetallic Pd–Pt catalysts: the influence of support materials. Appl Catal B Environ 66:175–185. https://doi.org/10.1016/J.APCATB.2006.03.010
87. Persson K, Ersson A, Jansson K, Iverlund N, Järås S (2005) Influence of co-metals on bimetallic palladium catalysts for methane combustion. J Catal 231:139–150. https://doi.org/10.1016/J.JCAT.2005.01.001
88. Gutiérrez-Guerra N, González-Cobos J, Serrano-Ruiz JC, Valverde JL, De Lucas-Consuegra A (2015) Electrochemical activation of Ni catalysts with potassium ionic conductors for CO2 hydrogenation. Top Catal 58:1256–1269. https://doi.org/10.1007/s11244-015-0488-4
89. González-Cobos J, Rico VJ, González-Elipe AR, Valverde JL, De Lucas-Consuegra A (2016) Electrocatalytic system for the simultaneous hydrogen production and storage from methanol. ACS Catal 6:1942–1951. https://doi.org/10.1021/acscatal.5b02844
90. Espinós JP, Rico VJ, González-Cobos J, Sánchez-Valencia JR, Pérez-Dieste V, Escudero C, de Lucas-Consuegra A, González-Elipe AR (2018) In situ monitoring of the phenomenon of electrochemical promotion of catalysis. J Catal 358:27–34. https://doi.org/10.1016/j.jcat.2017.11.027
91. De Lucas-Consuegra A, Caravaca A, González-Cobos J, Valverde JL, Dorado F (2011) Electrochemical activation of a non noble metal catalyst for the water-gas shift reaction. Catal Commun 15:6–9. https://doi.org/10.1016/j.catcom.2011.08.007
92. Panaritis C, Zgheib J, Couillard M, Baranova EA (2020) The role of Ru clusters in Fe carbide suppression for the reverse water gas shift reaction over electropromoted Ru/FeOx catalysts. Electrochem Commun 119:106824. https://doi.org/10.1016/j.elecom.2020.106824
93. Zagoraios D, Tsatsos S, Kennou S, Vayenas CG, Kyriakou G, Katsaounis A (2020) Tuning the RWGS reaction via EPOC and in situ electro-oxidation of cobalt nanoparticles. ACS Catal:14916–14927. https://doi.org/10.1021/ACSCATAL.0C04133
94. Leiva EPM, Vázquez C, Rojas MI, Mariscal MM (2008) Computer simulation of the effective double layer occurring on a catalyst surface under electro-chemical promotion conditions. J Appl Electrochem 38:1065–1073. https://doi.org/10.1007/S10800-008-9539-X/FIGURES/9
95. Pacchioni G, Lomas JR, Illas F (1997) Electric field effects in heterogeneous catalysis. J Mol Catal A Chem 119:263–273. https://doi.org/10.1016/S1381-1169(96)00490-6
96. Steinmann SN, Michel C, Schwiedernoch R, Filhol JS, Sautet P (2015) Modeling the HCOOH/CO2 electrocatalytic reaction: when details are key. ChemPhysChem 16:2307–2311. https://doi.org/10.1002/CPHC.201500187
97. Neophytides SG, Vayenas CG (1995) TPD and cyclic voltammetric investigation of the origin of electrochemical promotion in catalysis. J Phys Chem 99:17063–17067. https://doi.org/10.1021/j100047a001
98. Ladas S, Kennou S, Bebelis S, Vayenas CG (2002) Origin of non-faradaic electrochemical modification of catalytic activity. J Phys Chem 97:8845–8848. https://doi.org/10.1021/J100137A004
99. Tsampas MN, Sapountzi FM, Boréave A, Vernoux P (2013) Isotopical labeling mechanistic studies of electrochemical promotion of propane combustion on Pt/YSZ. Electrochem Commun 26. https://doi.org/10.1016/j.elecom.2012.09.043
100. Panaritis C, Hajar YM, Treps L, Michel C, Baranova EA, Steinmann SN (2020) Demystifying the atomistic origin of the electric field effect on methane oxidation. J Phys Chem Lett 11:6976–6981. https://doi.org/10.1021/acs.jpclett.0c01485
101. Tsiakaras P, Vayenas CG (1993) Non-faradaic electrochemical modification of catalytic activity: VII. The case of methane oxidation on platinum. J Catal 140:53–70. https://doi.org/10.1006/JCAT.1993.1068
102. Nicole J, Comninellis C, Tsiplakides D, Pliangos C, Verykios XE, Vayenas CG (2001) Electrochemical promotion and metal-support interactions. J Catal 204:23–34. https://doi.org/10.1006/jcat.2001.3360

103. Tauster SJ, Fung SC, Garten RL (1978) Strong metal-support interactions. Group 8 noble metals supported on titanium dioxide. J Am Chem Soc 100:170–175. https://doi.org/10.1021/ja00469a029
104. Tauster SJ, Fung SC, Baker RTK, Horsley JA (1981) Strong interactions in supported-metal catalysts. Science (80–) 211:1121–1125. https://doi.org/10.1126/science.211.4487.1121
105. Spichiger-Ulmann M, Monnier A, Koudelka M, Augustynski J (1986) Spectroscopic and electrochemical study of the state of Pt in Pt-TiO2 catalysts. ACS Symp Ser:212–227. https://doi.org/10.1021/BK-1986-0298.CH021
106. Tauster SJ (2002) Strong metal-support interactions. Acc Chem Res 20:389–394. https://doi.org/10.1021/AR00143A001
107. van Deelen TW, Hernández Mejía C, de Jong KP (2019) Control of metal-support interactions in heterogeneous catalysts to enhance activity and selectivity. Nat Catal 211(2):955–970. https://doi.org/10.1038/s41929-019-0364-x
108. Chen MS, Goodman DW (2007) Interaction of Au with titania: the role of reduced Ti. Top Catal 44:41–47. https://doi.org/10.1007/s11244-007-0276-x
109. Vernoux P, Guth M, Li X (2009) Ionically conducting ceramics as alternative catalyst supports. Electrochem Solid-State Lett 12. https://doi.org/10.1149/1.3122746
110. Katsaounis A, Nikopoulou Z, Verykios XE, Vayenas CG (2004) Comparative isotope-aided investigation of electrochemical promotion and metal-support interactions 1. 18O2 TPD of electropromoted Pt films deposited on YSZ and of dispersed Pt/YSZ catalysts. J Catal 222:192–206. https://doi.org/10.1016/j.jcat.2003.10.010
111. Li X, Gaillard F, Vernoux P (2007) Investigations under real operating conditions of the electrochemical promotion by O_2 temperature programmed desorption measurements. Top Catal 44. https://doi.org/10.1007/s11244-006-0131-5
112. Dole HAE, Safady LF, Ntais S, Couillard M, Baranova EA (2014) Improved catalytic reactor for the electrochemical promotion of highly dispersed Ru nanoparticles with CeO2 support. In: ECS transactions. Electrochemical Society, pp 65–74
113. Isaifan R, Dole H, Obeid E, Lizarraga L, Baranova EA, Vernoux P (2011) Catalytic CO oxidation over Pt nanoparticles prepared from the polyol reduction method supported on Yttria-stabilized zirconia. ECS Trans 35:43. https://doi.org/10.1149/1.3641818
114. Ntais S, Isaifan RJ, Baranova EA (2014) An X-ray photoelectron spectroscopy study of platinum nanoparticles on yttria-stabilized zirconia ionic support: insight into metal support interaction. Mater Chem Phys 148:673–679. https://doi.org/10.1016/J.MATCHEMPHYS.2014.08.033
115. Isaifan RJ, Ntais S, Couillard M, Baranova EA (2015) Size-dependent activity of Pt/yttria-stabilized zirconia catalyst for ethylene and carbon monoxide oxidation in oxygen-free gas environment. J Catal 324:32–40. https://doi.org/10.1016/j.jcat.2015.01.010
116. Dole HAE, Baranova EA (2016) Ethylene oxidation in an oxygen-deficient environment: why ceria is an active support? ChemCatChem 8:1977–1986. https://doi.org/10.1002/CCTC.201600142
117. Dole HAE, Costa ACGSA, Couillard M, Baranova EA (2016) Quantifying metal support interaction in ceria-supported Pt, PtSn and Ru nanoparticles using electrochemical technique. J Catal 333:40–50. https://doi.org/10.1016/j.jcat.2015.10.015
118. Isaifan RJ, Baranova EA (2015) Effect of ionically conductive supports on the catalytic activity of platinum and ruthenium nanoparticles for ethylene complete oxidation. Catal Today 241:107–113. https://doi.org/10.1016/j.cattod.2014.03.061
119. Dole HA, Kim JM, Lizarraga L, Vernoux P, Baranova EA (2012) Catalytic CO oxidation over au nanoparticles supported on Yttria-stabilized zirconia. ECS Trans 45:265. https://doi.org/10.1149/1.3701316
120. Hajar YM, Houache MSE, Tariq U, Vernoux P, Baranova EA (2017) Nanoscopic Ni interfaced with oxygen conductive supports: link between electrochemical and catalytic studies. ECS Trans 77:51–66. https://doi.org/10.1149/07710.0051ecst
121. Eluri R, Paul B (2012) Synthesis of nickel nanoparticles by hydrazine reduction: mechanistic study and continuous flow synthesis. J Nanopart Res 14. https://doi.org/10.1007/s11051-012-0800-1

122. González-Cobos J, López-Pedrajas D, Ruiz-López E, Valverde JL, de Lucas-Consuegra A (2015) Applications of the electrochemical promotion of catalysis in methanol conversion processes. Top Catal 58:1290–1302. https://doi.org/10.1007/s11244-015-0493-7
123. Khan MS, Lee SB, Song RH, Lee JW, Lim TH, Park SJ (2016) Fundamental mechanisms involved in the degradation of nickel–yttria stabilized zirconia (Ni–YSZ) anode during solid oxide fuel cells operation: a review. Ceram Int 42:35–48. https://doi.org/10.1016/J.CERAMINT.2015.09.006
124. Panaritis C, Yan S, Couillard M, Baranova EA (2021) Electrochemical study of the metal-support interaction between FeOx nanoparticles and cobalt oxide support for the reverse water gas shift reaction. J CO2 Util 101824. https://doi.org/10.1016/J.JCOU.2021.101824
125. Li K, Liu K, Ni H, Guan B, Zhan R, Huang Z, Lin H (2018) Electric field promoted ultra-lean methane oxidation over Pd-Ce-Zr catalysts at low temperature. Mol Catal 459:78–88. https://doi.org/10.1016/j.mcat.2018.08.021
126. He L, Fan Y, Bellettre J, Yue J, Luo L (2020) A review on catalytic methane combustion at low temperatures: catalysts, mechanisms, reaction conditions and reactor designs. Renew Sust Energ Rev 119:109589. https://doi.org/10.1016/J.RSER.2019.109589
127. Guan B, Lin H, Zhu L, Huang Z (2011) Selective catalytic reduction of NOx with NH3 over Mn, Ce substitution Ti0.9V0.1O2−δ nanocomposites catalysts prepared by self-propagating high-temperature synthesis method. J Phys Chem C 115:12850–12863. https://doi.org/10.1021/JP112283G
128. Roy S, Viswanath B, Hegde MS, Madras G (2008) Low-temperature selective catalytic reduction of NO with NH3 over Ti0.9M0.1O2-δ (M = Cr, Mn, Fe, Co, Cu). J Phys Chem C 112:6002–6012. https://doi.org/10.1021/JP7117086/SUPPL_FILE/JP7117086-FILE002.PDF
129. Zhao X, Xu D, Wang Y, Zheng Z, Li K, Zhang Y, Zhan R, Lin H (2021) Electric field assisted benzene oxidation over Pt-Ce-Zr nano-catalysts at low temperature. J Hazard Mater 407:124349. https://doi.org/10.1016/J.JHAZMAT.2020.124349
130. Shen F, Li K, Xu D, Li X, Zhao X, Chen T, Zhan R, Lin H (2019) Electric field promoted complete oxidation of benzene over PdCexCoy catalysts at low temperature. Catalysis 9:1071. https://doi.org/10.3390/CATAL9121071
131. Mo S, Zhang Q, Li J, Sun Y, Ren Q, Zou S, Zhang Q, Lu J, Fu M, Mo D, Wu J, Huang H, Ye D (2020) Highly efficient mesoporous MnO2 catalysts for the total toluene oxidation: oxygen-vacancy defect engineering and involved intermediates using in situ DRIFTS. Appl Catal B Environ 264:118464. https://doi.org/10.1016/J.APCATB.2019.118464
132. Shen F, Li K, Xu D, Yan R, Chen T, Zhan R, Lin H (2019) Electric field promoted oxidation of naphthalene over Cu/Ce0.55Zr0.45Ox catalysts at low temperature. Mol Catal 476:110536. https://doi.org/10.1016/J.MCAT.2019.110536
133. Li K, Xu D, Liu K, Ni H, Shen F, Chen T, Guan B, Zhan R, Huang Z, Lin H (2019) Catalytic combustion of lean methane assisted by an electric field over MnxCoy catalysts at low temperature. J Phys Chem C 123:10377–10388. https://doi.org/10.1021/ACS.JPCC.9B00496
134. Monyoncho EA, Zamlynny V, Woo TK, Baranova EA (2018) The utility of polarization modulation infrared reflection absorption spectroscopy (PM-IRRAS) in surface and: in situ studies: new data processing and presentation approach. Analyst 143:2563–2573. https://doi.org/10.1039/c8an00572a
135. Urakawa A, Bürgi T, Schläpfer HP, Baiker A (2006) Simultaneous in situ monitoring of surface and gas species and surface properties by modulation excitation polarization-modulation infrared reflection-absorption spectroscopy: CO oxidation over Pt film. J Chem Phys 124:054717. https://doi.org/10.1063/1.2159484
136. Hernandez WY, Hadjar A, Giroir-Fendler A, Andy P, Princivalle A, Klotz M, Marouf A, Guizard C, Tardivat C, Viazzi C, Vernoux P (2015) Electrochemically-assisted NOx storage-reduction catalysts. Catal Today 241:143–150. https://doi.org/10.1016/j.cattod.2014.03.076

137. Stavrakakis E, West M, Johnston S, McIllwaine R, Poulidi D (2019) Hydration, CO2 stability and wireless electrochemical promotion studies on yttria-doped Ba (Ce, Zr) O3 perovskites. Ionics (Kiel) 25:1243–1257. https://doi.org/10.1007/s11581-019-02836-6
138. Poulidi D, Thursfield A, Metcalfe IS (2007) Electrochemical promotion of catalysis controlled by chemical potential difference across a mixed ionic-electronic conducting ceramic membrane – an example of wireless NEMCA. Top Catal 44:435–449. https://doi.org/10.1007/s11244-006-0136-0
139. Poulidi D, Metcalfe IS (2008) Comparative studies between classic and wireless electrochemical promotion of a Pt catalyst for ethylene oxidation. J Appl Electrochem 388(38):1121–1126. https://doi.org/10.1007/S10800-008-9525-3
140. Poulidi D, Metcalfe IS (2010) In situ catalyst activity control in a novel membrane reactor-reaction driven wireless electrochemical promotion of catalysis. Chem Eng Sci 65:446–450. https://doi.org/10.1016/j.ces.2009.06.013
141. Poulidi D, Rivas ME, Zydorczak B, Wu Z, Li K, Metcalfe IS (2012) Electrochemical promotion of a Pt catalyst supported on La0.6Sr0.4Co0.2Fe0.8O3 − δ hollow fibre membranes. Solid State Ionics 225:382–385. https://doi.org/10.1016/J.SSI.2012.03.010
142. Poulidi D, Anderson C, Metcalfe IS (2008) Remote control of the activity of a Pt catalyst supported on a mixed ionic electronic conducting membrane. Solid State Ionics 179:1347–1350. https://doi.org/10.1016/J.SSI.2008.01.056
143. Poulidi D, Mather GC, Metcalfe IS (2007) Wireless electrochemical modification of catalytic activity on a mixed protonic–electronic conductor. Solid State Ionics 178:675–680. https://doi.org/10.1016/J.SSI.2007.02.022
144. Fuelcell Store (2022) Yttria-stabilized zirconia (8% Y). Standard Grade Powder
145. Inframat Advanced Materials (2022) 8 mol% yttria stabilized zirconia (YSZ) Nano Powder, 99.9+%, 30–60 nm
146. Lelalertsupakul W, Assabumrungrat S, Bumroongsakulsawat P (2020) Electrochemical promotion of propane oxidation at Pt/BiCuVOx-YSZ thin-film cells: economical use of YSZ. J Environ Chem Eng 8. https://doi.org/10.1016/j.jece.2020.104141